Key Points:

- Rain-snow levels (RSLs) are shallow in winter. In autumn and spring, RSLs span the full range of the profiling radar
- Rainfall microphysical characteristics and rates vary with RSLs
- RSLs determined from vertically profiling radar Doppler velocity correlate well with reanalysis derived melt levels

Correspondence to:

J. A. Shates,
shates@wisc.edu

Multi-Year Analysis of Rain-Snow Levels at Marquette, Michigan

J. A. Shates[1] [ID], C. Pettersen[2] [ID], T. S. L'Ecuyer[1] [ID], and M. S. Kulie[3] [ID]

[1]Department of Atmospheric and Oceanic Sciences, University of Wisconsin-Madison, Madison, WI, USA, [2]Department of Climate and Space Sciences and Engineering, University of Michigan, Ann Arbor, MI, USA, [3]Advanced Satellite Products Branch, NOAA/NESDIS/Center for Satellite Applications and Research, Madison, WI, USA

Abstract This study uses observations from a ground-based instrument suite to investigate the rain-snow level (RSL) in stratiform rainfall from January 2014 to April 2020 in the Upper Great Lakes Region. The height above the surface where ice melts to rain, the rain-snow level, influences microphysical assumptions in remote sensing precipitation retrievals and the ability of space-based radar to discriminate surface precipitation phase because of ground clutter. The instrument suite is installed at the Marquette, MI (MQT) National Weather Service station adjacent to Lake Superior. Rain events and the RSLs are studied through a ground-based vertically profiling radar (Micro Rain Radar), a custom NASA-developed video disdrometer (Precipitation Imaging Package), and reanalysis products from ECMWF ERA5 and NASA MERRA-2. Distinct macro and microphysical characteristics are observed in precipitation events with shallow RSLs (<1.8 km above ground level [AGL]) and intermediate RSLs (>1.8 km AGL). Intermediate RSLs correspond to rain events with relatively higher rain rates and a higher concentration of small drops in the drop size distributions (DSDs). Shallow RSL DSDs contain relatively higher concentrations of large drops with lower fall speeds suggesting that partially melted snowflakes may be reaching the surface. Reflectivity-rain-rate relationships are also impacted by microphysical differences associated with RSL regimes. Radar-detected RSLs agree with reanalysis-derived melt levels-especially at wet-bulb isotherms of 0.5°C and 1°C. Seasonal differences such as shallow RSLs in winter, fall, and spring have subsequent implications for satellite detectability.

Plain Language Summary The height above the surface where falling snow melts to rain, the rain-snow level (RSL), can be detected by both ground-based and space-based radars. However, space-based radars are limited in their ability to capture precipitation near the surface due to interference. This work investigates RSLs between January 2014 and April 2020 from ground-based observations at the Marquette, MI National Weather Service office. This work includes observations from ground-based profiling radar and a custom NASA-developed instrument that records high resolution videos of precipitation at the surface. In addition, profile temperature and moisture data are used. These products are commonly used with satellite observations to determine the surface precipitation phase. The results show different characteristics for rain events with shallow and intermediate RSLs. The radar-detected RSLs illustrate good agreement with melt levels derived from reanalysis profile data, which is useful for satellite retrievals of precipitation. Seasonal differences such as shallow rain-snow levels in winter, fall, and spring have subsequent implications for satellite detectability.

1. Introduction

Precipitation is changing as the climate warms. In northern mid and high latitudes, warming is resulting in a shift from snow to rain (Bintanja & Andry, 2017; Tamang et al., 2020). In the Upper Great Lakes region, the mean annual wet-bulb temperature is increasing, and snowfall and snowfall-precipitation ratio is decreasing (Tamang et al., 2020). Rainfall in the place of snowfall impacts water resources (Knowles et al., 2006), and glacier mass balance (Perry et al., 2017; Schauwecker et al., 2017), and potentially the global energy balance (Screen & Simmonds, 2012). Observed changes in precipitation including a reduction in heavy snow cover and the shift from snow to rain impacts soil moisture, watershed hydrology, and streamflow in the Midwest and Great Lakes region (Byun et al., 2019). From a societal standpoint, precipitation processes also impact transportation safety. Hazardous wintertime events such as freezing rain result in especially dangerous conditions that affect vehicle crash risks (Tobin et al., 2021). The height of the melting level in the atmosphere influences the precipitation phase at the surface (Cui et al., 2020; Harpold et al., 2017; White et al., 2002), and trends show increases in

melt level heights are linked to increasing rainfall and rainfall intensity as a result of surface warming (Prein & Heymsfield, 2020).

Satellites provide near-global observations and provide essential quantitative precipitation estimates for hydrometeorological applications on instantaneous/nowcasting to climate time scales. Accurate portrayals of surface precipitation phase from satellite retrievals are incredibly important, yet sometimes difficult to determine. Methods for separating rain and snow include radar profiles, surface measurements, and vertical profiles of temperature and relative humidity. Studies show that snowfall can occur at temperatures warmer than 4°C (Auer, 1974; Heymsfield et al., 2021), and freezing rain and mixed precipitation can exist at temperatures well below 0°C (Harpold et al., 2017; Stewart et al., 2015). In addition, surface type influences the temperature thresholds for rain and snow (Dai, 2008), and rain-snow temperature thresholds vary spatially (Jennings et al., 2018). Snowflakes falling through temperatures above 0°C may not melt depending on the relative humidity (Heymsfield et al., 2021; Matsuo & Sasyo, 1981). Moisture and pressure influence precipitation phase, and using wet bulb temperature (also referred to as ice-bulb temperature below 0°C) improves rainfall/snowfall discrimination (Behrangi et al., 2018; Ding et al., 2014) because the variable depends on temperature, pressure, and relative humidity. Atmospheric data in reanalysis products including temperature, relative humidity, wet bulb temperature, and near surface lapse rates can be used with other observations including radar to determine precipitation phase at the surface.

In addition to measured or model-derived meteorological variables, radar profile observations provide valuable information about precipitation phase. As snowflakes melt, relatively large ice hydrometeors become coated by liquid water and thus can produce a higher return in the reflectivity enhanced by a larger dielectric factor for liquid water (Austin & Bemis, 1950). This enhanced reflectivity is referred to as the radar bright band. Williams et al. (1995) classified precipitation from stratiform, mixed stratiform/convective, deep convective, and shallow convective clouds using Doppler radar variables from wind profilers in the tropics. White et al. (2002) developed an operational method using Doppler spectra from a network of vertically profiling radars in California to identify the radar bright band. Studies have explored implications for local hydrology (Henn et al., 2020; Lundquist et al., 2008; White et al., 2002), glaciology (Perry et al., 2017; Schauwecker et al., 2017), and microphysical differences between rain with and without a bright band (Lin et al., 2020; Martner et al., 2008). Methods for identifying melting through vertically profiling radar observations use variables including reflectivity (Cha et al., 2009), Doppler velocity (Perry et al., 2017), Doppler spectra skewness (Garcia-Benadi et al., 2020), and neural networks (Brast & Markmann, 2020). Weather radars employ other methods using dual polarization capabilities to identify melting (Giangrande et al., 2008; Matrosov et al., 2017; Ryzhkov & Zrnic, 2019).

Current satellite missions that provide valuable precipitation datasets include the Global Precipitation Measurement (GPM) Observatory (Hou et al., 2014; Skofronick-Jackson et al., 2017) and CloudSat (Stephens et al., 2008). GPM observes precip from 68°S to 68°N, while CloudSat observes from 82°S to 82°N. Different satellite products employ unique radar retrieval phase discrimination methods combining cloud/precipitation profile characteristics and reanalysis products. For Cloudsat, an inflection in reflectivity and attenuation can indicate the bright band in stratiform rainfall (Lebsock et al., 2020; Matrosov, 2010), while Liu (2008) employ a +2°C temperature threshold for snowfall/rainfall discrimination. For GPM Dual-Frequency Precipitation Radar (DPR), enhancements in the profile dual frequency ratios of reflectivity indicate bright bands (Chandrasekar & Le, 2020; Le et al., 2016). However, it remains challenging to get reliable precipitation measurements near the surface due to ground clutter. The satellite radar blind zone—radar observations directly above the surface that are affected by ground clutter—ranges from ∼700 m to over 2 km above the surface depending on surface type (e.g., ocean vs. land) and topography (Bennartz et al., 2019; Casella et al., 2017; Valdivia et al., 2022). In the case of shallow snowfall, satellite radars underestimate precipitation rate and occurrence (Maahn et al., 2014; McIlhattan et al., 2020). Satellite incidence angle has also been shown to affect observations resulting in underestimation of shallow precipitation (Hirose et al., 2021). In the case of rain falling at the surface, the satellite radar blind zone also poses an obstacle, masking vertical gradients in drop size and potentially obscuring liquid precipitation entirely when the melting level is shallow. Watters et al. (2018) showed that shallow bright bands were misidentified as surface clutter in GPM DPR resulting in retrievals above the melt layer. For passive sensors, such as the GPM Microwave Imager, surface type and snow cover contribute further to challenges in phase discrimination at the surface (Skofronick-Jackson et al., 2015). Skofronick-Jackson et al. (2019) showed that using the Sims and Liu (2015) method with wet-bulb temperature and near surface lapse rates reduced differences between GPM DPR and Cloudsat surface precipitation retrievals. GPM DPR overestimates snowfall, but using 2 m wet bulb

temperature from reanalyses improves phase discrimination (You et al., 2021). Also, there are ongoing updates and improvements to the GPM DPR phase discrimination and retrievals of precipitation rate (Hirose et al., 2021; Meneghini et al., 2021). New and upcoming satellite observing systems will enhance observations of clouds and precipitation and capture precipitation closer to the surface. In addition, planned satellite missions such as the Earth Clouds, Aerosol and Radiation Explorer (EarthCARE Illingworth et al., 2015) and the Atmospheric Observing System (AOS; https://aos.gsfc.nasa.gov/) are being designed with Doppler radar capabilities.

Ground-based radars—especially vertically pointing profiling radars—provide insights to near surface precipitation processes that may be obscured in the satellite radar blind zone. This work analyzes precipitation phase from the radar Doppler velocity by identifying and analyzing the height where ice melts to rain defined as the rain-snow level (RSL). The analysis provides insights to RSLs in the context of observing near surface precipitation within the satellite radar blind zone using Doppler radar capabilities. The following questions are addressed with the ultimate goal of providing robust datasets that can be used to evaluate satellite-derived surface precipitation phase and improve the accuracy of such retrievals: How do RSLs vary throughout the year? Do the macro and microphysical characteristics of rainfall events differ as a function of RSL? How can these observations be coupled with ancillary measurements such as reanalyses to better address uncertainties in remote sensing retrievals of surface precipitation type? A continuous, multi-year, multi-instrument site installed at the National Weather Service (NWS) Weather Forecast Office (WFO) in Marquette, Michigan provides a unique set of observations to examine precipitation phase and these questions in the Midwest region of the United States. Section 2 describes the instrumentation and data used in this work. Section 3 outlines the methodology used to identify RSLs from radar profile observations. Section 4 presents the radar RSL results and the macro and microphysical characteristics of the rainfall events. Section 5 expands upon results to address applications related to satellite-based rain rate retrievals and surface phase discrimination. Section 6 concludes and summarizes key points from the analysis.

2. Instrumentation and Data

This study uses observations from a continuous, multi-year suite of instruments at Marquette, MI (MQT; Kulie et al., 2021; Pettersen, Kulie, et al., 2020; Shates et al., 2022). The MQT instrument suite is located at the MQT NWS WFO, 13 km inland of Lake Superior and 426 m above sea level. The MQT NWS provides surface meteorological measurements including air and dew point temperature (2 m) and wind speed and direction (10 m) with 5-min resolution. In 2014, an enhanced snowfall instrument suite was installed, which includes a Micro Rain Radar and Precipitation Imaging Package (PIP). MQT observations have been used to explore cold season precipitation characteristics at MQT. Pettersen, Kulie, et al. (2020) examined snowfall regimes: shallow lake effect snow and deep synoptically forced snow. Kulie et al. (2021) further characterized MQT snowfall regimes, including enhancements of shallow and deep snowfall from the effects of orography and Lake Superior. The Great Lakes Region also experiences precipitation from atmospheric rivers (Mateling et al., 2021; Slinskey et al., 2020), and Mateling et al. (2021) illustrated that atmospheric river events impact the MQT site and often lead to enhanced precipitation rates and cold-season rain events.

2.1. Micro Rain Radar

The METEK MicroRain Radar 2 (MRR) is a 24 GHz (K band) vertically profiling frequency-modulated, continuous wave Doppler radar (Klugmann et al., 1996). The MRR is portable and relatively inexpensive, and uses relatively low power, which make it useful for observing precipitation across remote regions including mountainous sites and Antarctica (Cooper et al., 2022; Gorodetskaya et al., 2014; Kneifel et al., 2011; Schirle et al., 2019; Shates et al., 2021). The MRR was originally deployed and evaluated for measuring rainfall in remote regions (Maahn & Kollias, 2012; Peters et al., 2002). In addition, MRR observations have been used in identifying melting in stratiform rain (Brast & Markmann, 2020; Cha et al., 2009; Garcia-Benadi et al., 2020). The MRR observations were processed using the Maahn and Kollias (2012) method providing 1-min resolution of equivalent radar reflectivity (Z_e; dBZ), Doppler velocity (V_d; ms^{-1}) and spectral width (ms^{-1}). The processing also improves the sensitivity of the radar reflectivity to -10 dBZ. The operating range height of the radar is 3 km above ground level (AGL) and the range resolution is 100 m. Observations below 400 m AGL are removed due to ground clutter contamination, and 400 m AGL is defined as the near surface height bin. The stability of the MRR was assessed by comparing the 400 m AGL MRR reflectivities to NEXRAD radar reflectivities at approximately 400 m AGL (See Appendix A). The assessment supports that the MRR is stable in time.

2.2. Precipitation Imaging Package

The Precipitation Imaging Package (PIP) is a custom NASA video imager that uses a coupled bright light source and high speed camera to capture videos of shadows of falling hydrometeors (Newman et al., 2009; Pettersen, Bliven, et al., 2020; Pettersen et al., 2021). Image processing of these videos produce tables of hydrometeor microphysical characteristics at 1-min resolution, including drop size distributions (DSDs) and particle velocity distributions (VVDs). The PIP can resolve hydrometeors ranging from 0.4 to 26 mm with a 0.2 mm resolution. Additional processing provides an effective particle density and precipitation rates in liquid water equivalent (Pettersen, Bliven, et al., 2020). Additionally, the PIP can effectively discriminate precipitation phase (Pettersen et al., 2021).

2.3. Reanalyses

This study incorporates reanalysis products from European Centre for Medium-Range Weather Forecasts (ECMWF) ERA 5 (C3S, 2021; Hersbach et al., 2020) and the NASA Modern-Era Retrospective analysis for Research and Applications MERRA-2 (Gelaro et al., 2017). ERA5 has hourly temporal resolution, a spatial resolution of $0.25° \times 0.25°$, and a vertical resolution of 37 pressure levels. MERRA-2 has a 3-hourly temporal resolution, a spatial resolution of $0.5° \times 0.625°$, and 42 vertical pressure levels. We use vertical profiles of temperature and relative humidity at the nearest latitude and longitude coordinates to the MQT site: 46.5°N, 87.5°W.

Vertical profiles in reanalysis products are along pressure coordinates, but must be converted to height coordinates for radar profile comparisons. For MERRA-2, the edge height variable (edgeH) in units of m is used. The site elevation (426 m) was subtracted from the edge heights under the assumption that layer thicknesses (Bosilovich et al., 2016) are originally calculated from sea level. The ERA5 height coordinates are calculated using hydrostatic balance and the hypsometric equation (Petty, 2008) using 975 hPa as the surface level.

Profiles of wet bulb temperature are calculated iteratively from the profiles of temperature and relative humidity (Tamang et al., 2020) with the Brent (1973) optimization method. Vertical profiles of wet bulb temperature are linearly interpolated to increase temperature resolution to 0.01°C also improving the height resolution. The wet bulb temperature can be used to define the melt level in the profile (Cui et al., 2020; Harpold et al., 2017; Heymsfield et al., 2021; Prein & Heymsfield, 2020; Sankaré & Thériault, 2016; Stewart et al., 2015).

3. Methods

As snowflakes melt to rain drops, they fall faster toward the surface (Atlas et al., 1973). This is apparent in the Doppler velocity (V_d) of a vertically profiling radar where the V_d is greater for rainfall than snowfall. In the column above the radar, the transition from snow to rain is associated with a distinct V_d increase and is evident in the gradient of the V_d with respect to height (Lin et al., 2020; Pfaff et al., 2014; White et al., 2002; Williams et al., 1995). In this work, we define the RSL based on a peak inflection in the V_d gradient, which is where the melting is the strongest (Lin et al., 2020). The RSL generally appears below the radar reflectivity indicated bright band. In addition, the bright band height determined by the dual-frequency reflectivity ratio from the GPM DPR has also been shown to agree well with melt level heights derived from V_d (Lebsock et al., 2020).

The rain and RSL identification starts with a threshold for precipitation occurrence of radar reflectivity greater than −10 dBZ at the 400 m AGL (Kulie et al., 2021; Mateling et al., 2021; Pettersen, Kulie, et al., 2020; Shates et al., 2021). Next, rain and snow are separated using a V_d threshold (White et al., 2002) where rain is conservatively categorized as having V_d greater than 3 ms^{-1}. This surface phase identification was tested and verified with multiple snow-rain transition events using the PIP particle effective density product, which accurately discriminates rain versus snow (Pettersen et al., 2021). Figure 1a shows observations from the MRR and PIP during a rain to snow transition event. Surface precipitation phase from the effective density shows a shift from rain to mixed precipitation to snow. The detection of the RSL corresponds to raining periods detected by the PIP. Additionally, Pettersen et al. (2021) show that the PIP effective density product compares well with methods described by Sims and Liu (2015) that use surface wet bulb temperature and near surface lapse rates to determine surface snowfall probability.

Figure 1b contains an example of a V_d profile and corresponding V_d gradients with respect to height (the derivative of V_d with respect to height is designated as dV_d) from an April rain event. Using the peak change in the gradient
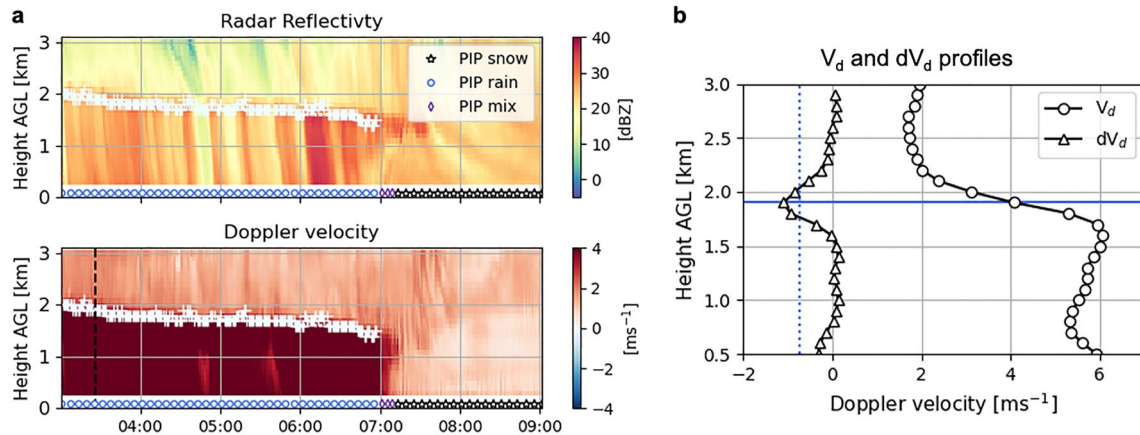
Figure 1. Methods summary and example of rain-snow level (RSL) identification. (a) Radar reflectivity and Doppler velocity time series are shown for a rain to snow transition event at Marquette, MI on 10 April 2015. The RSLs are plotted on the radar reflectivity and Doppler velocity as white + symbols. The Precipitation Imaging Package phase observed at the surface is superimposed on to the radar time series. The black, dashed vertical line in the Doppler velocity time series indicates the time of the profile explored in the plot to the right. (b) The V_d and dV_d are shown. The dV_d threshold is plotted as a blue, dashed vertical line. The blue, solid horizontal line shows the height of the identified RSL for that minute.

of the V_d profile to detect melting has been shown effective in stratiform precipitation (Lin et al., 2020; Pfaff et al., 2014; White et al., 2002; Williams et al., 1995). White et al. (2002) defined a threshold of $-7.14 \times 10^3 \, \text{s}^{-1}$ ($-1.5 \, \text{ms}^{-1}/210 \, \text{m}$) to flag melting in the V_d profile. For this study, the threshold value to identify the height of the RSL is $-7.5 \times 10^{-3} \, \text{s}^{-1}$ ($-0.75 \, \text{ms}^{-1}/100 \, \text{m}$). The threshold was determined empirically to effectively separate profiles with and without melting in the MRR range, and accounts for the MRR range resolution (100 m). Additionally, the RSL is calculated for downward moving velocities only (toward the radar); any upward motions are ignored. For flagged rain associated with melting in the range of the radar, more than 90% of the peak dV_d magnitudes exceed the threshold. The RSLs were also evaluated against NEXRAD-identified RSLs for 550+ coincident minutes of rainfall during 19 different days. The cross correlation coefficient (ρ_{HV}) from scanning radars can be used to identify melting (Gatlin et al., 2018; Giangrande et al., 2008; Matrosov et al., 2017; Ryzhkov & Zrnic, 2019). We used scans between 6° and 10° in order to avoid ground clutter contamination. The NEXRAD ρ_{HV} and MRR RSLs are in good agreement with differences in values within the range resolution of the MRR (figure not shown).

Rain events without a melting signature within the operating range height of the radar (3 km AGL) were flagged as undetected when the following criteria were met: the minimum V_d was greater than 3 ms^{-1} throughout the profile and continuous radar reflectivity values were greater than -10 dBZ throughout the profile up to 3 km AGL. These rain events are likely associated with melting above 3 km AGL. The undetected category may also include instances of rainfall without a discernible RSL. Warm rain or shallow convective rainfall, which are rare at this site, would not be flagged at all, as the dV_d threshold would not be met and precipitation echo tops would be too shallow for the continuous radar reflectivity criteria.

In Section 5, we use MRR RSLs to evaluate the reanalysis derived melt levels from ERA5 and MERRA-2. The temporal resolution for ERA5 is hourly and MERRA-2 is 3-hourly, while the MRR observations are 1-min resolution. To compare the observations to reanalyses with different temporal resolutions, we use a 25-min threshold to flag hours. For flagged RSL hours, we compute the mean RSL to represent the full hour. We then match the hours of the flagged MRR-determined RSL with the corresponding 3-hourly MERRA-2 time resolution. The 3-hourly resolution is used to compare the mean MRR RSL, ERA5, and MERRA-2 hr.

4. Results

4.1. Analysis of MRR Rain-Snow Levels

The RSLs at MQT vary throughout the year. Figure 2 shows the annual distribution of RSLs as a box and whisker plot and half violin plots (empirical distributions of the data) for all precipitation events when a RSL is observed below 3 km AGL. The summer months (JJA) have consistently higher RSLs (>2 km AGL), with the values in
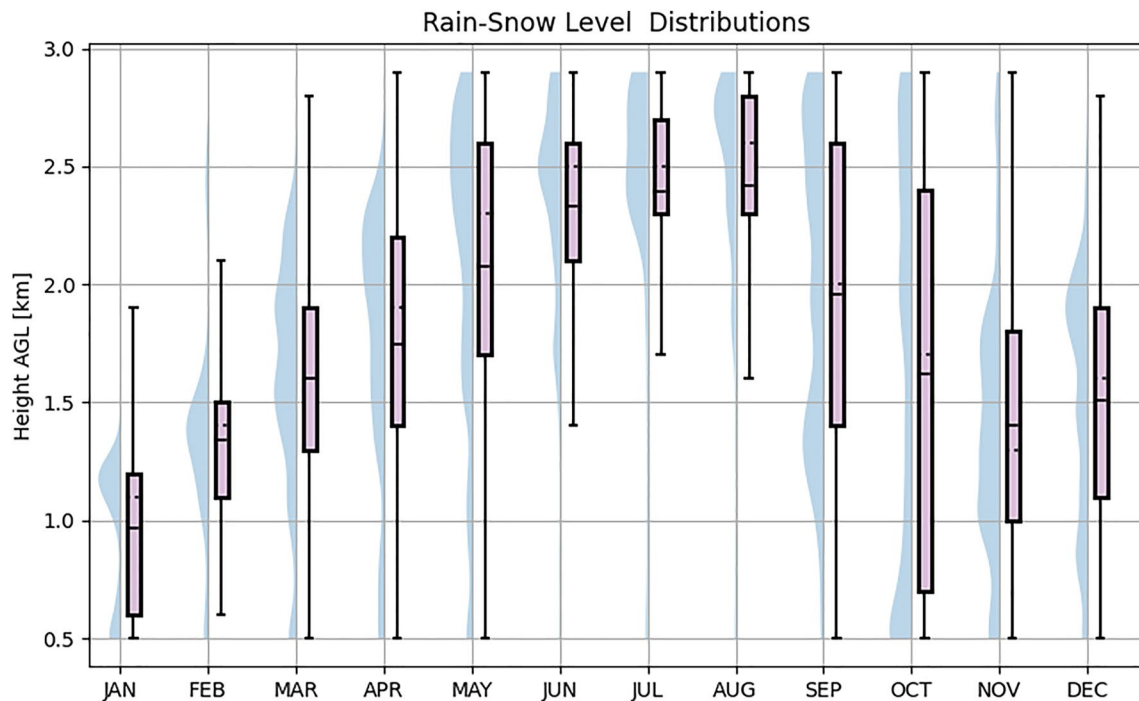
Figure 2. Distribution of rain-snow levels. The boxes include the 25th to 75th percentile of the data and the whiskers span from the 5th to the 95th percentile. The solid lines show the mean values and the black dotted line/point shows the median. To the left of each box, there are half violin plot showing the empirical distribution of the data for that month.

July and August primarily above 2.5 km AGL. RSLs during winter months (NDJF) occur closer to the surface (RSL < 2 km AGL). The mean RSL is the lowest in January at 0.9 km AGL, while the distribution for December is the highest out of the winter months. The transition season months (MAM and SON) exhibit substantial spread in the RSLs ranging from 0.5 to 3 km AGL. May and October are the two rainiest months in MQT (See Table B2) and both have the largest RSL range between the 25th and 75th percentile (0.7–2.4 km AGL). However, the half violin plots show that October distribution is concentrated below 1 km AGL, whereas the May distribution has a higher distribution above 2 km AGL.

Loosely guided by the vertical resolutions of spaceborne radars (250–500 m), the RSLs are separated into four height ranges to assess whether macro and microphysical characteristics depend on RSL: 0.6–1.2, 1.2–1.8, 1.8–2.4, and 2.4–3 km AGL. Table 1 summarizes the frequency of occurrence during the full observation period (January 2014–April 2020) for the observed height categories. During the observational period, 72,290 surface rain minutes were detected by the MRR, with 53,139 flagged as containing a rain-snow transition. For the 26.5% of occurrences without a detected transition, RSLs above 3 km AGL are likely. In June–September, approximately 40%–65% of the rainfall events did not have a discernible transition in the range of the radar (Table A1). The high instance of non-detection in the summer supports that the melting occurred above the operating range height of the radar. The 2.4–3 km height category has the highest percentage of rainfall with a RSL (22.3%). The 0.6–1.2 km height category has the lowest frequency of occurrence at 9.44%. The event hours listed in the summary table (Table 1) show the number of hours that are represented in each category for reanalysis comparisons. The order of increasing number of hours with increasing RSL matches with the increasing percent occurrence for the entire observation period.

4.2. Macro and Microphysical Characteristics of Rainfall

As snow falls and melts to rain, the radar reflectivity and Doppler velocity observed by the radar changes with height. Figure 3 contains two-dimensional histograms that composites all rain events observed with flagged RSLs in the MRR for the separate height categories. The presence of a bright band
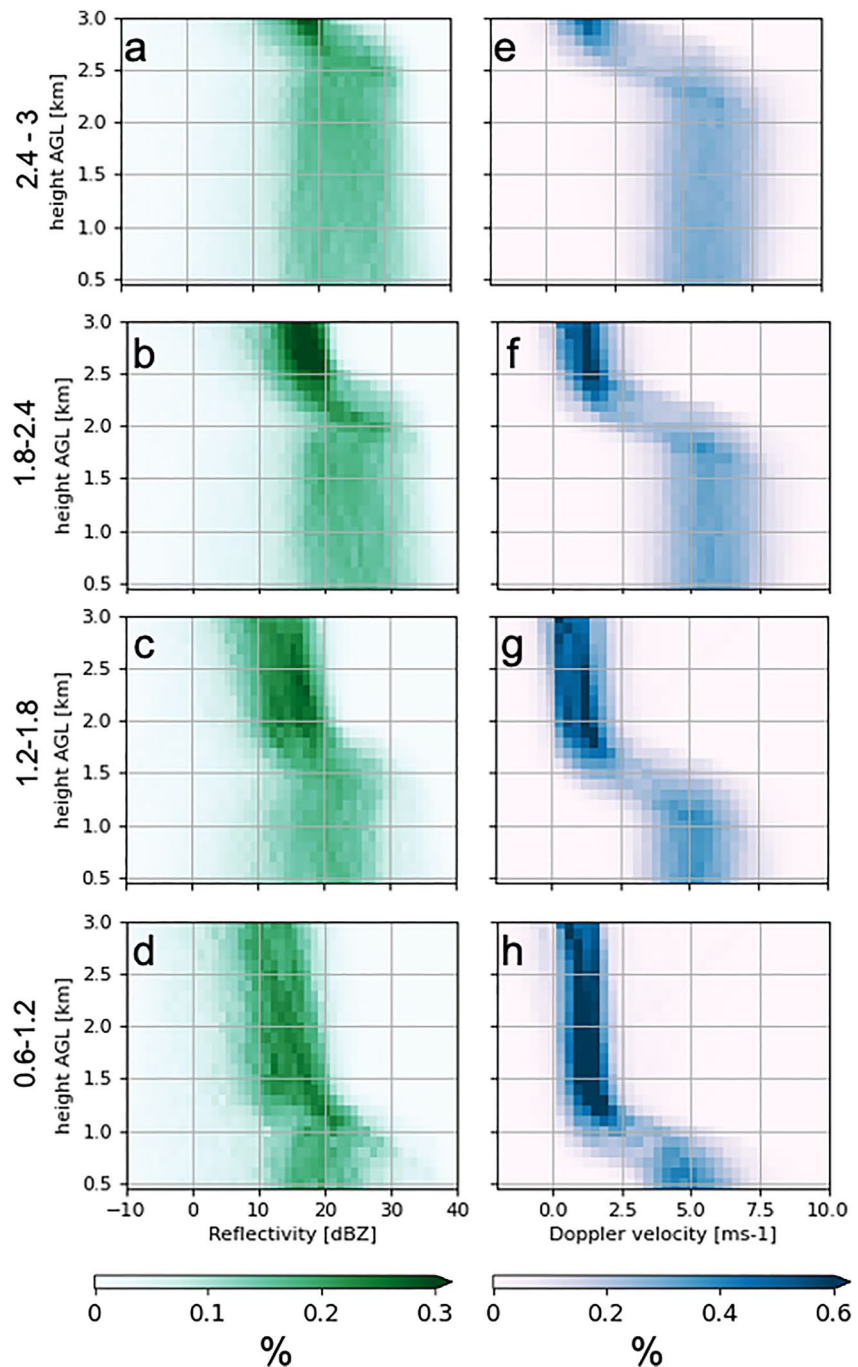
Table 1
Rain-Snow Level Summary

Height categoryAGL [km]	0.6–1.2	1.2–1.8	1.8–2.4	2.4–3	Undetected
Percent occurrence	9.44	15.6	17.59	22.3	26.5
Event hours	31	53	61	85	X

Figure 3. Two dimensional histograms of radar profiles of reflectivity and Doppler velocity from all rain events from observational period. Radar profiles are shown in subplots separated by Rain-snow levels height categories: 0.6–1.2 km (a), (e), 1.2–1.8 km (b), (f), 1.8–2.4 km (c), (g), 2.4–3 km (d), (h). The histograms are normalized by total number of observations for each height category.

is apparent with an increase followed by a decrease in reflectivity with decreasing height for height categories (Figures 3a–3d). For RSLs above 1.8 km AGL, the range of snowfall reflectivities are narrower (10–20 dBZ at heights above 1.8 km AGL) than for the near-surface rainfall reflectivities. Near the surface, reflectivities range from 15 dBZ to greater than 30 dBZ (Figures 3a and 3b). Reflectivity gradually increases toward the RSL (above bright band for the reflectivity) for height category 1.2–1.8 km AGL and 0.6–1.2. For height category 0.6–1.2 km AGL, the reflectivities of snowfall above the melting layer have a broader range from 5 to 18 dBz compared to

the other height categories. The reflectivities near the surface occur between 10 and 25 dBZ for the lowest height category (Figure 3d). Near the surface, the mean reflectivity values are 17.8, 18.55, 21.9, and 21.79 dBZ for the four height categories 0.6–1.2 km, 1.2–1.8 km, 1.8–2.4 km, 2.4–3 km AGL respectively.

The snowfall above the RSL has a relatively narrow range of V_d values ranging from 0 to ∼2.4 ms^{-1} for all height categories. Below the RSL, the V_ds increase and the range in V_d broadens (Figures 3e–3h), which also corresponds to a broadening and increase in spectral width right below the RSL (not shown). The V_d does not continue to broaden toward the surface after the initial broadening associated with the RSL. The near surface V_ds for RSLs 0.6–1.2 and 1.2–1.8 km AGL range from 3 to 6 ms^{-1} (Figures 3g and 3h). with mean values of 5.2 and 5.4 ms^{-1}. The near surface V_d for transitions above 1.8 km AGL have the highest occurrence of values exceeding 5 ms^{-1}. The mean V_ds are 5.8 and 5.8 ms^{-1} for the height categories 1.8–2.4 and 2.4–3 km AGL. The highest RSL category (2.4–3 km AGL) has V_ds exceeding 7 ms^{-1}.

Figure 4 contains observations of the PIP microphysical characteristics for each RSL height category. In the mean DSDs, there are differences in the concentrations of small drops and large drops for RSL height categories (Figure 4a). For the two RSL height categories above than 1.8 km AGL, there is a larger concentration of drops with diameters between 1 and 2 mm than for RSLs above 1.8 km AGL. The DSDs for RSLs below 1.8 km AGL have higher concentrations of drops greater than 2 mm. The shallowest RSL category (0.6–1.2 km AGL) has the highest concentration of drops larger than 2.5 mm compared to the other height categories.

The mean PIP-derived fall speeds for the RSL categories are similar for drop diameters smaller than 2 mm (Figure 4b), and they follow the expected curve for the terminal velocity of rain drops increasing drop size with increasing fall speed (Atlas & Ulbrich, 1977; Atlas et al., 1973; Uplinger, 1981). For drops larger than 2 mm, a separation in fall speeds emerges between the RSL height categories. Shallower RSL events have lower fall speeds for the same equivalent diameter drops. Hydrometeors in the lowest RSL height category (0.6–1.2 km AGL) do not exceed fall speeds of 7 ms^{-1}, and fall speeds continue to decrease for particles larger than 3 mm. The PIP may be observing frozen or partially melted particles, or large deformed drops, and this is further discussed in Section 5.1.2. The highest RSL category (2.4–3 km AGL) contains drops with fall speeds greater than 8 ms^{-1}.

Higher RSL height categories are observed to have higher rain rates (Figure 4c). All RSL categories contain a distribution with a high concentration of low rain rates. The one-dimensional histogram shows that for the lowest detected RSLs (0.6–1.2 km AGL), the PIP observes rain rates up to 5 mmh^{-1}. The next height category has a higher number of observations of low rain rates, and the PIP measures rates up to 6 mmh^{-1}. Rain rates reach up to 8 mmh^{-1} for precipitation transitions between 1.8 and 2.4 km AGL, and RSL values between 2.4 and 3 km AGL have the highest rain rates, reaching 10 mmh^{-1}.

The near-surface MRR reflectivity values and corresponding PIP rain rates are compared for the RSL height categories in the two-dimensional histograms shown in Figure 5. For RSLs above 1.8 km AGL, there are a larger number of rain rates exceeding 1 mmh^{-1} and near surface reflectivity is dominated by values greater than 20 dBZ (Figures 5c and 5d). Rain events with RSLs below 1.8 km AGL are dominated by rain rates less than 1 mmh^{-1} (Figures 5a and 5b). The RSLs between 0.6 and 1.2 km AGL have the highest concentration of near-surface reflectivities between 10 and 25 dBZ (Figure 5a).

5. Discussion

5.1. Seasonality and the Satellite Radar Blind Zone

Rain-snow levels vary seasonally at MQT from January 2014 to April 2020. The results show that the winter months have lower RSLs, occurring below 2 km AGL. During shoulder-season months, we see the largest spread in RSLs (Figure 2). We found that for approximately 40% of the raining events with a detected RSL (27% for all rain events detected) the RSL was below 2 km AGL. RSLs respond to the seasonal change in temperature. During the cold season, most precipitation falls as snow at MQT, but Mateling et al. (2021) showed that atmospheric river events reaching the site increase the likelihood of rainfall. Surface air temperatures associated with many shallow RSL rainfall events were also near 0°C (not shown), which further underlines the challenge in using a temperature threshold to separate snow, rain-snow transitions, and freezing rain (Stewart et al., 2015) within the satellite radar blind zone.
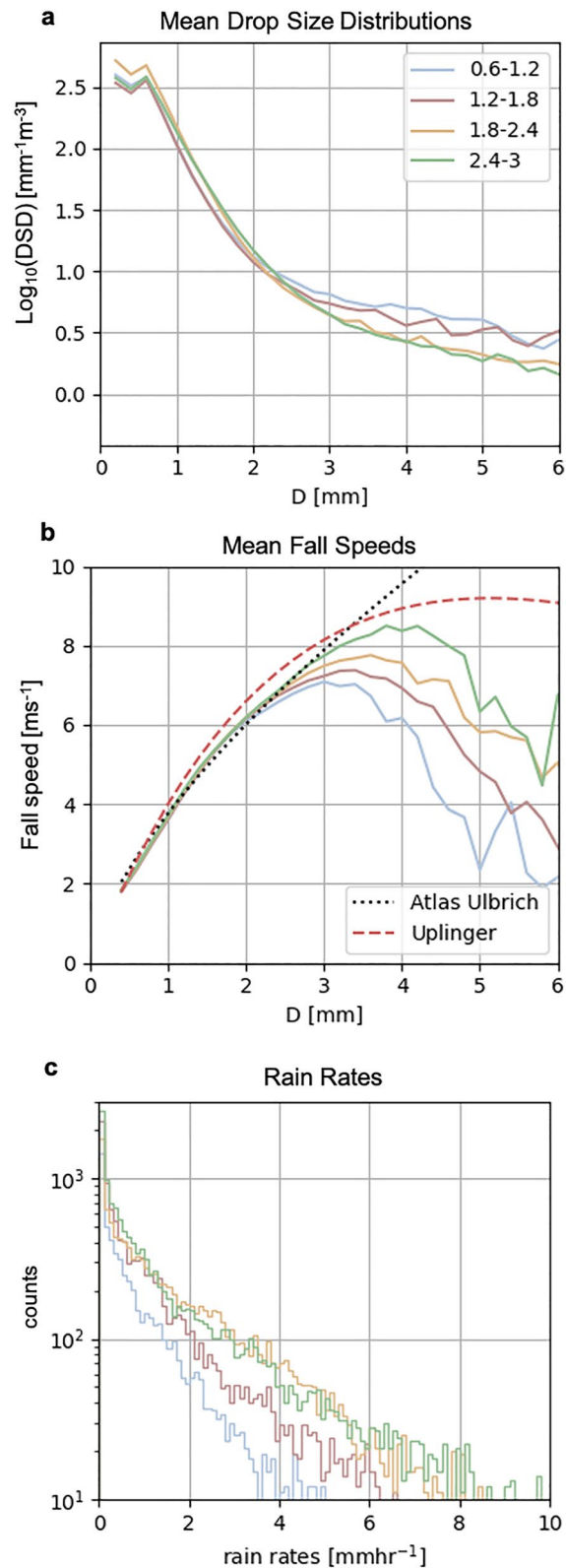
Figure 4. Precipitation Imaging Package results for Rain-snow level height categories (1.2–1.8, 1.8–2.4, and 2.4–3 km above ground level) including (a): mean drop size distributions, (b) mean fall speeds, (c) one dimensional histogram of rain rates. In (b), the terminal velocity as a function of drop size are included as a black, dotted line for Atlas and Ulbrich (1977), and red, dashed line for Uplinger (1981) as described by Serio et al. (2019).
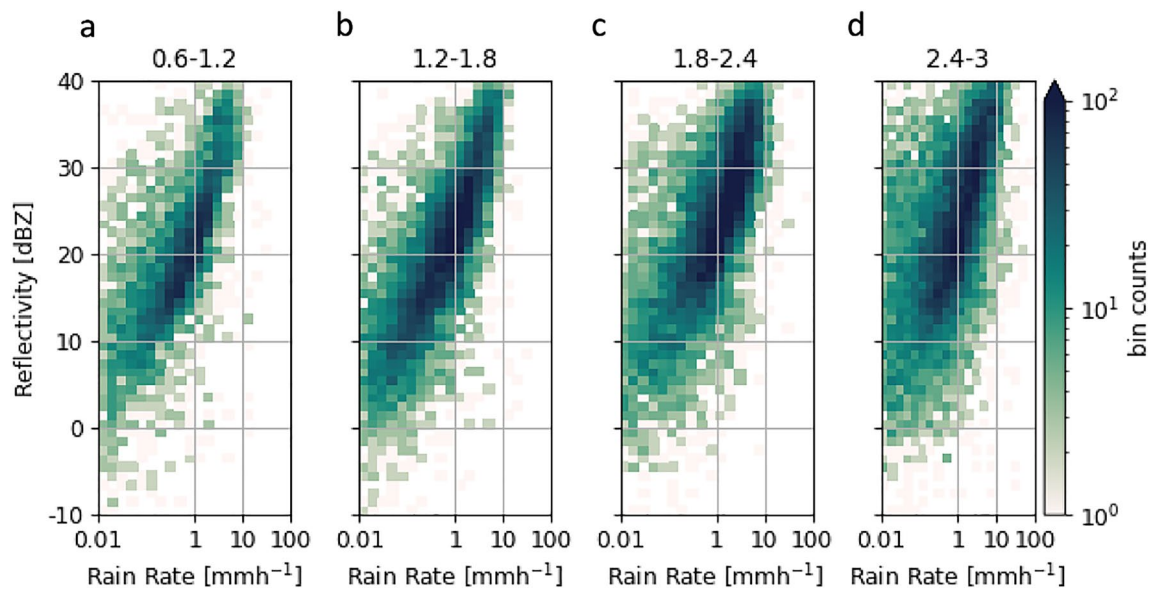
Figure 5. Two dimensional histograms of Precipitation Imaging Package rain rates in relation to Micro Rain Radar (MRR) near surface reflectivity for separate Rain-snow level height categories above ground level (AGL): (a), 1.2–1.8 km (b), 1.8–2.4 km (c), 2.4–3 km (d). The MRR near surface reflectivity is defined at 400 m AGL because ground clutter can impact MRR observations below 400 m AGL.

Depending on surface type and the signal of the precipitation, the satellite radar blind zone ranges 720 m to 2 km (Bennartz et al., 2019; Casella et al., 2017), and over land in non-mountainous regions, measurements may be difficult to observe below 1.25 km. For CloudSat, attenuation from melting contributes to uncertainties with DSDs and precipitation retrievals (Matrosov, 2010). In GPM DPR, shallow melt layers result in poor phase classification in the winter (Pejcic et al., 2020), and the shallow bright band can be misidentified as ground clutter (Watters et al., 2018). In addition, scanning weather radars may also be affected by shallow melting layers, as radar beams intersecting the melting layer are affected by attenuation (von Lerber et al., 2014). Weather radars may also overshoot the melting layer due to range and beam curvature effects (Norin et al., 2015, 2017; Pettersen, Kulie, et al., 2020; Watters et al., 2018), Also, ground clutter obscures detection of shallow melting layers in weather radar (Giangrande et al., 2008).
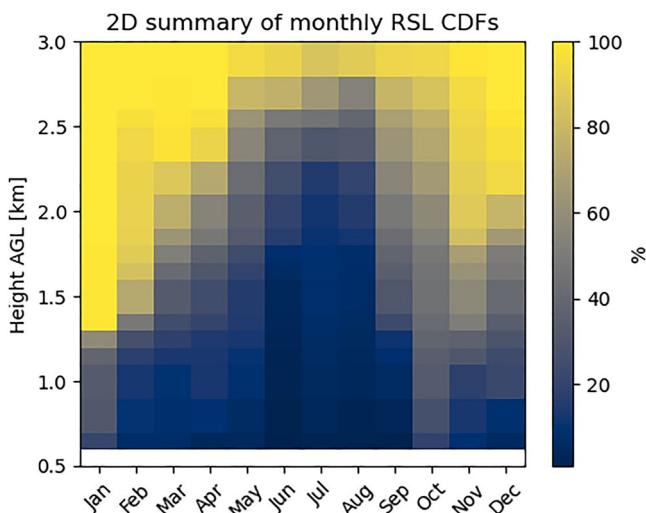

Figure 6. Monthly cumulative distribution functions for all detected Rain-snow level from January 2014 to April 2020. The distributions are expressed as percents.

Figure 6 contains a two-dimensional composite of monthly cumulative distribution functions (CDFs) for the RSLs. The monthly CDFs show the percentages of the RSLs observed below each 100 m bin resolution for each month of the year (resolution of the MRR). The 2D CDF summary provides insights into the fraction of scenes for which the RSL may be difficult to observe through a space-based radar as a function of blind zone depth. In January, effectively 100% of the melting layers occur below 1.5 km AGL. More than 60% of the RSLs in February are observed below 1.5 km AGL. In December, approximately 40% of the RSLs are below 1.5 km AGL. As spring months progress toward summer months, the CDFs decrease with increasing height, indicating that there are higher RSLs in the distribution even though there are some shallow transitions (Figure 2). Beginning with September, the CDFs show that the melt levels are closer to the surface for a higher percentage of the observations, although the spread is still large (Figure 2).

The results of the RSL height categories show a separation in the macro and microphysical characteristics of rainfall with RSLs above and below 1.8 km AGL. The following discussion will describe the RSLs as shallow for height categories below 1.8 km AGL (RSL: 0.6–1.2 km and 1.2–1.8 km AGL) and intermediate for RSLs above 1.8 km AGL (RSL: 1.8–2.4 and 2.4–3.0 km

AGL). The term intermediate reflects the fact these RSLs are not shallow, but are also within the range of the radar, which is limited to below 3 km AGL.

5.1.1. Intermediate Rain-Snow Levels

Rain-snow levels above ∼2 km AGL are likely to be correctly identified by spaceborne radars, as they are generally occurring above the blind zone, depending on surface type and presence of orography (Bennartz et al., 2019; Casella et al., 2017). Watters et al. (2018) showed that phase detection in GPM DPR was better in summer months than winter months because of the relatively higher bright bands. The MRR reflectivity profiles show that there is a notable increase in reflectivity associated with the RSL (Figures 3a and 3b), and retrievals using reflectivity gradients would capture the RSL. The PIP rain rates corresponding to the near-surface MRR reflectivities are concentrated greater than 1 mmh^{-1} for the intermediate height categories (Figures 5c and 5d). PIP observations show that these rain events also tend to have higher rain rates that exceed 6 mmh^{-1} (Figure 4c). Correspondingly, higher melting levels have been shown to be associated with higher rain rates (Henn et al., 2020; Prein & Heymsfield, 2020).

The microphysical characteristics of intermediate height categories suggest precipitation processes occurring below the RSL. The surface-based observations of DSDs for intermediate height categories contain a higher concentration of small drops (effective diameters between 1 and 2 mm). The high concentration of small drops suggests the occurrence of drop breakup as the rain drops fall below the melt level. As the rain drops fall, they collide and break up resulting in more and smaller drops (List & Gillespie, 1976). Prein and Heymsfield (2020) describe that increasing melt levels results in an increase in warm rain processes including collision and coalescence. The high number concentration of small drops is consistent with heavier rainfall associated with a higher melt level. Other in situ or remote sensing measurements would be needed to further explore the processes occurring as the drops fall.

5.1.2. Shallow Rain-Snow Levels

Rain-snow levels below 1.8 km AGL may pose a challenge for spaceborne remote sensing retrievals of rain rate, due the likelihood of occurring within the satellite radar blind zone (Bennartz et al., 2019; Casella et al., 2017; Pejcic et al., 2020; Watters et al., 2018). The occurrence of RSL is also valuable to assess in a warming climate with a shift from snow to rain in northern latitudes (Tamang et al., 2020) due to increasing melt level heights (Prein & Heymsfield, 2020). In addition, melting heights decrease with increasing latitude (Cannon et al., 2017; Lundquist et al., 2008), which suggests that changes from snowfall to rainfall in high latitudes may be challenging to observe within the satellite radar blind zone.

During the shallow RSL events, the MRR reflectivities near the surface range from 10 to greater than 20 dBZ. The reflectivity of the snowfall above the melt level remains below 20 dBZ (Figures 3c and 3d). Above the RSL, the MRR reflectivity two-dimensional histograms show that the reflectivities associated with snowfall steadily increase with decreasing height. While the radar reflectivity magnitude is likely affected by attenuation above the melting level, the steady increase with decreasing height may suggest aggregation processes (Field, 2000; Shates et al., 2021) prior to melting. Dolan et al. (2022) explored microphysical processes of precipitation cases through dual-polarized scanning radar observations; in regions where the snowflake habit above the bright band was identified as aggregates there was a steady increase in reflectivity above the bright band. Also, snowfall characteristics such as snow density are useful for melting layer models in quantitative precipitation estimation with weather radars (von Lerber et al., 2014). The range of near-surface reflectivities for these RSL rain events have lower values compared to the intermediate RSL height categories, and the PIP observed rain rates are concentrated below 1 mmh^{-1} (Figures 5a and 5b).

Proximity of the RSL to the surface impacts the DSDs and fall speeds of hydrometeors. The DSDs for the shallow RSL height categories contain a larger concentration of drops with diameters greater than 3 mm compared to the intermediate RSL height categories, and even drops as large as 6 mm are observed (Figure 4a). The occurrence of these larger hydrometeors is consistent with there being less time and distance for the drops to break up into smaller drops, as the melt level is much closer to the ground (List & Gillespie, 1976; Stewart et al., 2015; Yuter et al., 2006). Gatlin et al. (2018) showed that lower and thicker melting layers resulted in larger rain drops in observed DSDs. The PIP also observed that fall speeds start to decrease for drops larger than 3 mm (decreasing from 6 ms^{-1} to less than 4 ms^{-1}). One possibility is that the PIP is observing large deformed droplets where the droplet deformation is affecting fall speeds (Wang & Pruppacher, 1977). Yuter et al. (2006)

showed the occurrence of large rain drops (effective diameters > 6 mm) in mixed precipitation events using PARSIVEL disdrometer measurements. These large drops were formed from aggregates that had melted, but did not have time or distance to break up. Also, larger hydrometeors with the lower fall speeds may suggest that some of these shallow RSL events contain mixed precipitation that is reaching the surface. The habit of the ice crystals above the melting layer can also influence the distance required to fully melt ice particles (Sankaré & Thériault, 2016; Stewart et al., 2015), and the mass of the snowflakes impacts the DSDs of the rain drops (Dolan et al., 2022; Fujiyoshi & Muramoto, 1996). Lee et al. (2020) also found that the microphysical characteristics of snowfall above the bright band influenced the size and concentrations of rain drops at the surface. Above the melt level, the increasing reflectivity with decreasing height suggests that many of these rain events may have snow aggregation occurring aloft (Dolan et al., 2022; Field, 2000; Shates et al., 2021) particularly as the temperature increases toward melting (Lamb & Verlinde, 2011) leading to potentially large, partially melted aggregates/wet snow reaching the surface.

5.2. Remote Sensing Applications

5.2.1. *Z-R* Relationships

In order to obtain a precipitation rate from a radar reflectivity value, it is necessary to use a reflectivity (Z) to rain rate (R) relationship. A *Z-R* power law relationship and coefficients are influenced by the microphysical characteristics of rainfall including the number density, size and fall speeds of rain drops (Atlas et al., 1973; Steiner et al., 2004). Satellite radar precipitation retrievals used with GPM DPR depend on precipitation phase discrimination to assume a DSD for rain or particle size distribution for snowfall including stratiform versus convective assumptions (Skofronick-Jackson et al., 2019). There are differences in stratiform and convective rainfall microphysical characteristics that affect precipitation retrievals (Bringi et al., 2003; Steiner et al., 2004). In addition, Martner et al. (2008) and Lin et al. (2020) report differences in the *Z-R* relationships between bright band and non bright band stratiform rainfall due to microphysical processes (collision and coalescence only vs. melting snowflakes grown through ice processes).

From the near-surface MRR reflectivity values and PIP rain rates, we are able to obtain empirically derived *Z-R* relationships. Figure 7 shows operational *Z-R* relationships, empirical RSL *Z-R* relationships, and mean PIP rain rates for MRR reflectivity bins. The operational *Z-R* include: $Z = 130R^2$ Cool Season (east) Stratiform, $Z = 200R^{1.6}$ Marshall Palmer Stratiform, $Z = 300R^{1.4}$ Summer Deep Convective (NWS, 2015). These specific *Z-R* relations are applied to NEXRAD observations, which are S-band (~10 cm wavelength). The empirical MRR-PIP *Z-R* are $Z = 133R^{2.1}$, $Z = 83R^{2.5}$, $Z = 50R^{2.7}$, $Z = 101R^{2.2}$ for RSL height categories 0.6–1.2, 1.2–1.8, 1.8–2.4, and 2.4–3 km AGL respectively. While the MRR and NEXRAD do not operate at the same frequency, both mostly observe liquid precipitation in the Rayleigh scattering regime. Possible non-Rayleigh effects for the K-band radar observations are likely limited to very intense precipitation events that are rarely observed at MQT, especially for stratiform rainfall with relatively low melting levels. The mean rain rates from the PIP and the corresponding *Z-R* curves for the shallow RSL height categories (RSL < 1.8 km AGL) are distinct from the Marshall Palmer *Z-R* relationship for stratiform rain, but match well with the *Z-R* relationship used by the NWS at MQT, the cool season (east) stratiform *Z-R* (Figures 7a and 7b). The fall speeds and the DSDs suggest the presence of some wet snow (Figures 4a and 4b), but the *Z-R* is still effective for these shallow RSLs (e.g., Licznar and Krajewski (2016) showed that rain and rain with wet snow *Z-R* resemble each other).

Figures 7c and 7d shows that the PIP mean rain rates and the *Z-R* relationships for the intermediate RSL height categories (RSL > 1.8 km AGL) do not match the existing *Z-R* relationships used for cool season stratiform rain, nor the Marshall Palmer stratiform rain, nor deep convective rain used at the Chicago, Illinois NWS NEXRAD radar (KLOT). The two intermediate RSL height categories (1.8–2.4 and 2.4–3 km) also have different *Z-R* relationships. The rain rates for RSLs 2.4–3.0 km AGL have higher rain rates than those between 1.8 and 2.4 km for a reflectivity range of 15 and 25 dBZ. However, rain rates for reflectivities greater than 25 dBZ are higher RSLs between 1.8 and 2.4 km. The unique *Z-R* relationships are likely a result of the distinct microphysical characteristics (e.g., DSDs; Figure 4a). The DSDs and *Z-R* relationships suggest that accounting for the height of the melting level may be important for radar retrievals of precipitation.
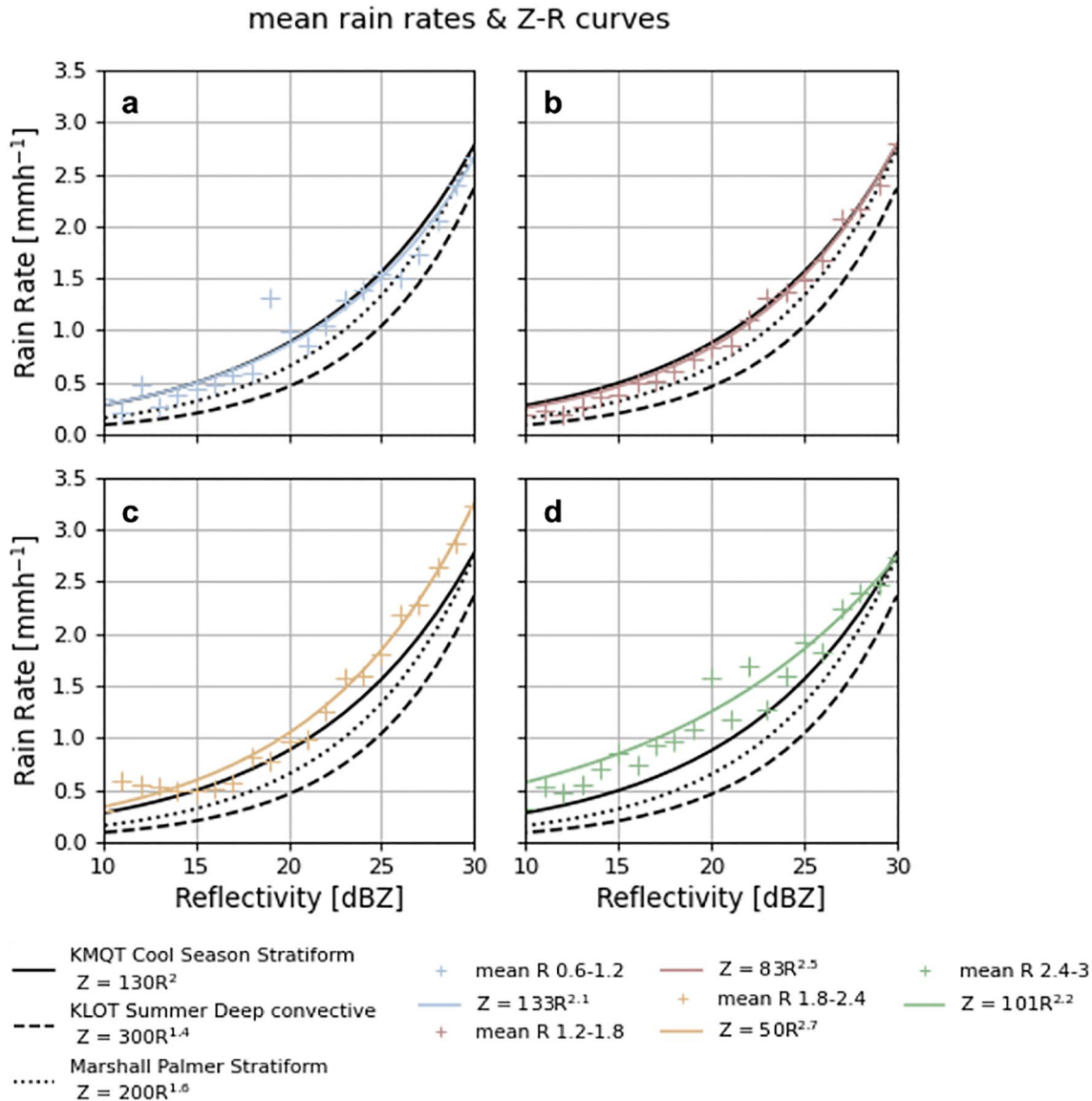
Figure 7. *Z-R* curves calculated from near surface Micro Rain Radar reflectivity and Precipitation Imaging Package rain rates for each height category 0.6–1.2 km (a), 1.2–1.8 km (b), 1.8–2.4 km (c), 2.4–3 km (d). The mean rain rates are calculated for 21 reflectivity bins ranging from 10 to 30 dBZ. The *Z-R* curves were obtained from the mean rain rates between 10 and 30 dBZ. In this reflectivity range, there were a minimum of 100 rain rates (minutes) per reflectivity bin. The mean rain rates and corresponding *Z-R* relations are compared to *Z-R* relations used with NWS Doppler weather radars (WSR-88D): Marshall Palmer Stratiform, Cool Season Stratiform at Marquette, MI (KMQT), and Summer Deep Convective at Chicago, IL (KLOT).

5.2.2. Evaluation of Profile Wet Bulb Temperature

Reanalysis products are commonly used with satellite radar observations to determine surface precipitation phase and retrieve snow or rain rates (e.g., Lebsock et al., 2020; Liu, 2008; Skofronick-Jackson et al., 2019; You et al., 2021). The CloudSat precipitation products use reflectivity attenuation to separate convective and stratiform precipitation, and the melting (freezing) level to separate solid and liquid precipitation (Lebsock et al., 2020). The ECMWF temperature and humidity profiles are used for the melt layer model in CloudSat products (Haynes et al., 2009). Vertical profiles of temperature and relative humidity from reanalysis products provide these ancillary data. Here, we define reanalysis melt levels (ML) at the 0°C, 0.5°C and 1°C isotherms using profiles of wet-bulb temperature (T_w) calculated from ERA5 and MERRA-2 temperature and relative humidity profiles. The number of hours included from each RSL height category in this analysis are outlined in Table 1. The MRR RSLs and ERA5 MLs are matched up with the 3-hourly resolution of MERRA-2 MLs.
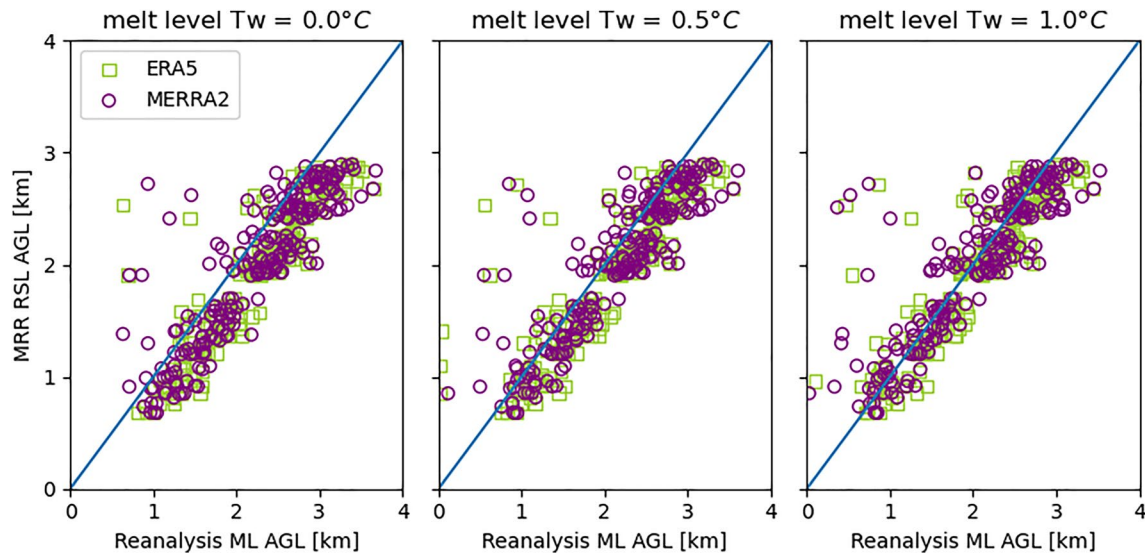
Figure 8. Scatter plots of melt levels from ERA5 and MERRA-2 reanalyses against Micro Rain Radar (MRR) rain-snow levels. The one-to-one line is shown in blue. The subplots compare MRR rain-snow level (RSL) and the height in the profile where the wet bulb temperature is 0°C (a), 0.5°C (b) and 1°C (c). When there is a temperature inversion in the profile resulting in multiple instances of 0°C, 0.5°C, and 1°C, then the highest occurrence represents the melt level. Pearson correlation coefficients between the Rain-snow level and melt levels from ERA5 and MERRA-2 are shown in each plot.

The vertical structure of temperature during a precipitation event largely controls the surface phase (Harpold et al., 2017; Sims & Liu, 2015; Stewart et al., 2015). The T_w profile (i.e., ML) provides additional information for phase discrimination by identifying the onset of melting (Figure 8). Figures 8a–8c contains scatter plots comparing the MRR RSLs and the MLs at T_w of 0°C, 0.5°C and 1°C. There is high correlation between the MRR RSLs and MLs for all three of the T_w. Generally, the RSL occurs below the ML, which is consistent with the fact that the snow particles gradually melt through the melt layer, and the distance to fully melt depends on the microphysical characteristics of the snowfall (Stewart et al., 2015; White et al., 2002). The mode differences between the reanalysis ML and MRR RSL (reanalysis ML—MRR RSL) at the 1°C ML are 0 m for MERRA2 and 100 m for ERA5, respectively. For the 0.5°C and 1°C ML, there are an increasing number of points above the one-to-one line indicating that some of the reanalysis MLs are flagged below the RSL (Figures 8b and 8c). At the 0.5°C ML, both ERA5 and MERRA-2 have mode differences of 200 m. Compared to the 0°C ML, the points for the 0.5°C and 1°C ML are closer to the one-to-one line for both reanalysis MLs. The mode differences for MERRA-2 0°C range between 200 and 400 m, while the mode for the ERA5 0°C difference is 300 m. ERA5 has a higher Pearson correlation coefficient than MERRA-2 between the MRR RSL and the ML (≥0.88), but the correlation is still high for MERRA-2 for all of the ML (≥0.85). In general, the RSLs and MLs appear to agree the most at T_w of 1°C for ERA5 and MERRA-2.

Knowing how the RSL (or reflectivity bright band height) compare to the melting level is valuable for forecasting models (Henn et al., 2020) and for satellite precipitation retrievals (Lebsock et al., 2020; Sims & Liu, 2015). For 19 vertically profiling radars on the west coast of the US, there was a ±250 m bias between the modeled melt level (temperature of 0°C) and the radar detected bright band (Henn et al., 2020). Cui et al. (2020) showed that surface $T_w = 0.5$°C was the best threshold for separating rain and snow along mountain-sides. Lundquist et al. (2008) showed that there was a difference of −400 to 200 m between the radar snow level and the surface rain-snow transition, but the difference varied between locations. At a mountainous site and coastal site in South Korea, Cha et al. (2009) found the error between the bright band height and radiosonde freezing level height was 329 and 367 m, respectively. On average, White et al. (2002) showed the rawinsonde melting level was 192 m above the radar bright band. Cannon et al. (2017) investigated space-based bright band heights from GPM DPR with MERRA-2 freezing levels over the west coast of the US and over the eastern Pacific for atmospheric river events, and found that there was good agreement with a mean difference of 356 m. In the same study, Cannon et al. (2017) found that the mean absolute error between GPM-DPR bright band heights and the ground-radar network was 284 m. Schauwecker et al. (2017) compared reanalysis freezing levels to MRR snow level heights in the tropical Andes, and that MRR-derived levels were 240 m (220 m) below MERRA-2 (ERA-Interim) reanalysis

levels. While these numerous studies use different methods in identifying melting in the radar and defining melting levels (dry bulb vs. wet bulb temperature), our results are consistent with the difference between the RSL and ML from previous studies.

6. Conclusions

This study illustrates the annual distribution of RSLs over Marquette, Michigan from January 2014 to April 2020, and the associated micro and macro physical characteristics of rainfall at the surface. Additionally, applications of RSL height categories are assessed against Z-R relationships and retrieval assumptions using reanalysis data products. The work combines ground-based vertically profiling radar, surface video disdrometer measurements, and reanalysis products for analyses of the rainfall characteristics as a function of RSL.

Vertically profiling Doppler radar observations were used to identify RSLs throughout the year. The results illustrate a seasonal cycle in the height of the RSLs with shallow RSLs (below 1.8 km AGL) occurring in winter months and intermediate RSLs (above 1.8 km AGL) in summer months. Seasonal transition months, for example, May and October, showed substantial spread in RSL, ranging from below 1 km AGL and up to 3 km AGL. The shallow RSLs in winter, spring and fall (particularly below 1 and 1.5 km AGL) may be challenging to detect using current space-based radar observations, while future missions should consider optimizing radar capabilities to more effectively identify shallow melt layers. These results highlight a need to investigate satellite bright band height and thickness in winter and seasonal transition months over mid-latitude ground-based sites. In addition, the shallow RSLs could potentially be missed or impact observations by ground-based scanning weather radars. Understanding the signature of melting in Doppler radar profiles is relevant for future satellite observing systems including EarthCARE and AOS, which will be able to detect vertical motions in clouds and precipitation with Doppler capabilities. Future studies could continue to explore RSLs in the Great Lakes Region with the MRR, NEXRAD weather radar at MQT, GPM DPR bright band heights, CloudSat rain products, and upcoming missions.

Near-surface radar observations and microphysical characteristics show differences for rain with shallow versus intermediate RSLs. Intermediate RSL rainfall have higher near-surface reflectivity and Doppler velocity values. Microphysical characteristics show that DSDs have larger concentrations of small drops (effective diameter <2 mm) and higher rain rates for intermediate RSLs. For the shallow RSLs, there are relatively more large hydrometeors (effective diameter >3 mm) in the DSDs, but slower fall speeds indicating that these rain events may also include partially melted snowflakes (mixed-phase precipitation) or large deformed drops.

From the PIP and MRR observations, we empirically derived and compared the reflectivity to rain rate (Z-R) relations for rainfall from different RSL height categories. For both shallow RSL categories (<1.8 km AGL), the Z-R curves are similar to the Z-R relation used for the NWS S-Band weather radar (KMQT) in cool season stratiform rain. The empirically derived Z-R curves for the intermediate height categories (RSL >1.8 km AGL) were distinct from cool season stratiform rain, the Marshall Palmer stratiform rain, and also deep convective Z-R relations used for multiple NWS radars. The operational Z-R curves indicate that the relations are underestimating rainfall from the intermediate RSLs.

This study explored reanalysis-derived melt levels associated with rainfall at MQT. Profiles of wet-bulb temperature were derived from MERRA-2 and ERA5 profiles of temperature and relative humidity to obtain melt levels at 0°C, 0.5°C and 1°C isotherms. We compare RSLs to reanalysis melt levels, and show especially high agreement heights at 0.5°C and 1°C.

RSLs were investigated at a site in the Upper Great Lakes Region with implications for satellite detectability of rainfall near the surface. Shallow RSLs are likely to be particularly challenging for satellite radars to detect and may be an increasing area of interest with the warming climate and a shift from snow to rain in the mid and high latitudes. In addition, impactful precipitation events such as atmospheric rivers are responsible for warm, intense precipitation in the Midwest and may be further linked to rain in the cold seasons. The insights presented in this work are valuable for the planning and designing any future satellite radars in consideration of the satellite radar blind zone.

Appendix A: Micro Rain Radar and NEXRAD

The radar reflectivity values from the MRR and NEXRAD are compared for 7 rain events (1 per year) from January 2014 to April 2020. The MRR is frequently used in remote locations for studying precipitation without ways to assess how the radar performs over time, and this comparison allows us to assess the stability of the MRR over time. Reflectivities from the 400 m AGL height bin are used from the MRR. To obtain NEXRAD observations at a similar height bin, we use reflectivities in the 2.4° elevation scan at a range of 10 km from the radar. The horizontal scans from the NEXRAD do not include observations directly above the MRR because the MRR is adjacent (50 m) to the weather radar and is in the radar cone of silence. It is also important to note that the NEXRAD observations are from a horizontal volume scan and will include spatial differences in precipitation (which is why the distributions are not a one-to-one match). To work with the NEXRAD observations, we used the Python Atmospheric Radiation Measurement (ARM) Radar Toolkit Py-ART (Helmus & Collis, 2016). Importantly, the distributions from the respective radars indicate that the MRR calibration is stable over the 7 year period and the reflectivity values do not drift (Figure A1) In addition, the reflectivities from the two radars are comparable suggesting that the MRR reflectivities are largely unbiased. Table A1 shows that the median reflectivities for the events are similar for the MRR and NEXRAD. For most events, the difference between the radar medians are within 2 dB of each other.
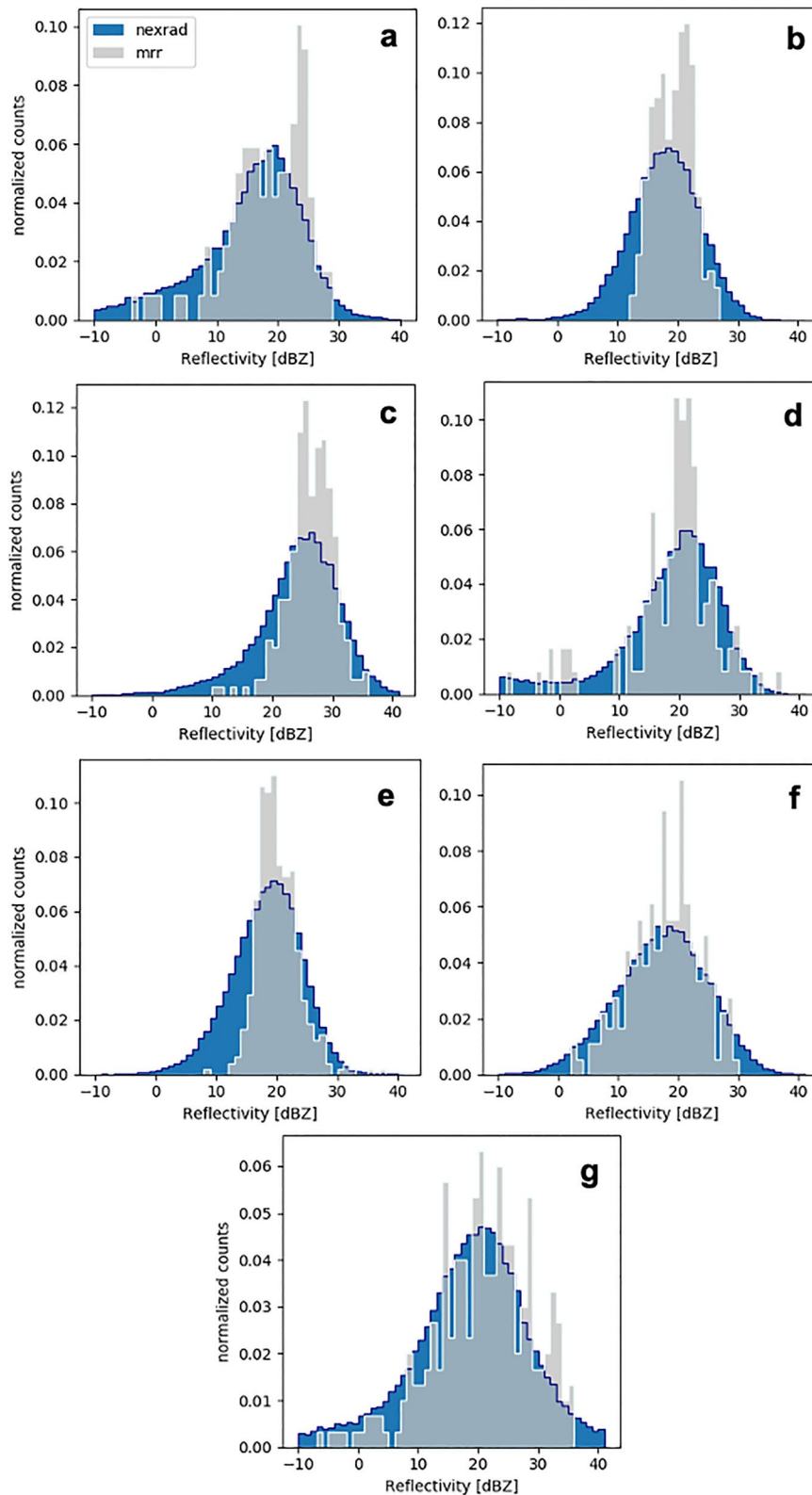
Figure A1. Normalized distributions of radar reflectivities from the NEXRAD and Micro Rain Radar (MRR) at MQT. MRR reflectivites are at 400 m above ground level, and the NEXRAD reflectivities are from the 2.4° elevation scan at 10 km range from the radar. Each distribution is from a different example event per year during within the observation period: (a) 7 June 2014, 22–24 UTC; (b) 30 May 2015, 1–6 UTC; (c) 4 June 2016, 13–18 UTC; (d) 29 June 2017, 0–2 UTC; (e) 8 October 2018, 0–5 UTC; (f) 10 June 2019, 7–10 UTC; (g) 4 April 2020, 4–9 UTC.

Table A1
Median Reflectivity Values for Each Event for MRR and NEXRAD

Event	MRR	NEXRAD
7 June 2014 22–24 UTC	18.75	16.5
30 May 2015 1–6 UTC	19.36	17.5
4 June 2016 13–18 UTC	26.37	24.5
29 June 2017 0–2 UTC	19.82	19.0
8 October 2018 14–22 UTC	18.73	18.5
10 June 2019 7–10 UTC	17.98	17.0
4 April 2020 4–9 UTC	20.37	19.0

Appendix B: Rain Summary

This section contains tables for occurrence and minutes for each month during the study period. Table B1 shows percent of rain per month where melting was not detected and melting likely occurred above 3 km AGL. Table B2 summarizes the total number of minutes for rain per month observed January 2014–April 2022 for RSLs and rain with undetected RSLs. These total minutes do not include shallow convective rainfall.

Table B1
Rain Occurrence With Undetected Rain-Snow Level January 2014–April 2020

Jan	0.00%
Feb	0.00%
Mar	2.26%
Apr	1.99%
May	12.18%
Jun	47.23%
Jul	66.89%
Aug	55.72%
Sep	43.61%
Oct	17.26%
Nov	7.75%
Dec	0.09%

Table B2
Total Rain Minutes Per Month Including Rain With and Without a Detected RSL

Jan	887
Feb	1,238
Mar	2,789
Apr	6,898
May	11,099
Jun	9,298
Jul	5,008
Aug	6,989
Sep	8,476
Oct	11,617
Nov	3,343
Dec	4,648

Data Availability Statement

Ground-based remote-sensing observations from the Micro Rain Radar and Precipitation Imaging Package hosted at the Marquette, MI National Weather Service Office have been uploaded to an online data repository (https://doi.org/10.5281/zenodo.7325232). NEXRAD data for Marquette were accessed August 2022 and were downloaded from the NOAA National Centers for Environmental Information. The Python Atmospheric Radiation Measurement (ARM) Radar Toolkit Py-ART was used to work with NEXRAD observations (https://doi.org/10.5334/jors.119). ERA5 data were downloaded from the Copernicus Climate Data Store (CDS) and were accessed in February 2022. MERRA-2 data were downloaded from the NASA Goddard Earth Sciences Data and Information Services Center and were accessed in February 2022.

References

Atlas, D., Srivastava, R., & Sekhon, R. S. (1973). Doppler radar characteristics of precipitation at vertical incidence. *Reviews of Geophysics*, *11*(1), 1–35. https://doi.org/10.1029/rg011i001p00001

Atlas, D., & Ulbrich, C. W. (1977). Path-and area-integrated rainfall measurement by microwave attenuation in the 1–3 cm band. *Journal of Applied Meteorology and Climatology*, *16*(12), 1322–1331. https://doi.org/10.1175/1520-0450(1977)016<1322:paairm>2.0.co;2

Auer, A. H., Jr. (1974). The rain versus snow threshold temperatures. *Weatherwise*, *27*(2), 67. https://doi.org/10.1080/00431672.1974.9931684

Austin, P. M., & Bemis, A. C. (1950). A quantitative study of the "bright band" in radar precipitation echoes. *Journal of the Atmospheric Sciences*, *7*(2), 145–151. https://doi.org/10.1175/1520-0469(1950)007<0145:aqsotb>2.0.co;2

Behrangi, A., Yin, X., Rajagopal, S., Stampoulis, D., & Ye, H. (2018). On distinguishing snowfall from rainfall using near-surface atmospheric information: Comparative analysis, uncertainties and hydrologic importance. *Quarterly Journal of the Royal Meteorological Society*, *144*(S1), 89–102. https://doi.org/10.1002/qj.3240

Bennartz, R., Fell, F., Pettersen, C., Shupe, M. D., & Schuettemeyer, D. (2019). Spatial and temporal variability of snowfall over Greenland from cloudsat observations. *Atmospheric Chemistry and Physics*, *19*(12), 8101–8121. https://doi.org/10.5194/acp-19-8101-2019

Bintanja, R., & Andry, O. (2017). Towards a rain-dominated arctic. *Nature Climate Change*, 7(4), 263–267. https://doi.org/10.1038/nclimate3240

Bosilovich, M., Lucchesi, R., & Suarez, M. (2016). *Merra-2: File specification GMAO office note no. 9 (version 1.1)*. GMAO Greenbelt.

Brast, M., & Markmann, P. (2020). Detecting the melting layer with a micro rain radar using a neural network approach. *Atmospheric Measurement Techniques*, *13*(12), 6645–6656. https://doi.org/10.5194/amt-13-6645-2020

Brent, R. P. (1973). *Algorithms for minimization without derivatives, Chap. 4*. Prentice-Hall.

Bringi, V., Chandrasekar, V., Hubbert, J., Gorgucci, E., Randeu, W., & Schoenhuber, M. (2003). Raindrop size distribution in different climatic regimes from disdrometer and dual-polarized radar analysis. *Journal of the Atmospheric Sciences*, *60*(2), 354–365. https://doi.org/10.1175/1520-0469(2003)060<0354:rsdidc>2.0.co;2

Byun, K., Chiu, C.-M., & Hamlet, A. F. (2019). Effects of 21st century climate change on seasonal flow regimes and hydrologic extremes over the midwest and great lakes region of the US. *Science of the Total Environment*, *650*, 1261–1277. https://doi.org/10.1016/j.scitotenv.2018.09.063

C3S. (2021). Era5: Fifth generation of ECMWF atmospheric reanalyses of the global climate. *Copernicus Climate Change Service Climate Data Store (CDS), date of access = March 2021*.

Cannon, F., Ralph, F. M., Wilson, A. M., & Lettenmaier, D. P. (2017). GPM satellite radar measurements of precipitation and freezing level in atmospheric rivers: Comparison with ground-based radars and reanalyses. *Journal of Geophysical Research: Atmospheres*, *122*(23), 12–747. https://doi.org/10.1002/2017jd027355

Casella, D., Panegrossi, G., Sanò, P., Marra, A. C., Dietrich, S., Johnson, B. T., & Kulie, M. S. (2017). Evaluation of the GPM-DPR snowfall detection capability: Comparison with cloudsat-CPR. *Atmospheric Research*, *197*, 64–75. https://doi.org/10.1016/j.atmosres.2017.06.018

Cha, J.-W., Chang, K.-H., Yum, S. S., & Choi, Y.-J. (2009). Comparison of the bright band characteristics measured by micro rain radar (MRR) at a mountain and a coastal site in South Korea. *Advances in Atmospheric Sciences*, *26*(2), 211–221. https://doi.org/10.1007/s00376-009-0211-0

Chandrasekar, V., & Le, M. (2020). Dpr dual-frequency precipitation classification. In *Satellite precipitation measurement* (pp. 193–210). Springer.

Cooper, S. J., L'Ecuyer, T. S., Wolff, M. A., Kuhn, T., Pettersen, C., Wood, N. B., et al. (2022). Exploring snowfall variability through the high-latitude measurement of snowfall (HiLaMS) field campaign. *Bulletin of the American Meteorological Society*, *103*(8), E1762–E1780. https://doi.org/10.1175/bams-d-21-0007.1

Cui, G., Bales, R., Rice, R., Anderson, M., Avanzi, F., Hartsough, P., & Conklin, M. (2020). Detecting rain–snow-transition elevations in mountain basins using wireless sensor networks. *Journal of Hydrometeorology*, *21*(9), 2061–2081. https://doi.org/10.1175/jhm-d-20-0028.1

Dai, A. (2008). Temperature and pressure dependence of the rain-snow phase transition over land and ocean. *Geophysical Research Letters*, *35*(12). https://doi.org/10.1029/2008gl033295

Ding, B., Yang, K., Qin, J., Wang, L., Chen, Y., & He, X. (2014). The dependence of precipitation types on surface elevation and meteorological conditions and its parameterization. *Journal of Hydrology*, *513*, 154–163. https://doi.org/10.1016/j.jhydrol.2014.03.038

Dolan, B., Rutledge, S. A., & Rasmussen, K. L. (2022). Multiscale interactions contributing to enhanced orographic precipitation in landfalling frontal systems over the Olympic Peninsula. *Monthly Weather Review*, *150*(6), 1207–1231. https://doi.org/10.1175/mwr-d-21-0160.1

Field, P. R. (2000). Bimodal ice spectra in frontal clouds. *Quarterly Journal of the Royal Meteorological Society*, *126*(563), 379–392. https://doi.org/10.1002/qj.49712656302

Fujiyoshi, Y., & Muramoto, K. (1996). The effect of breakup of melting snowflakes on the resulting size distribution of raindrops. *Journal of the Meteorological Society of Japan. Series II*, *74*(3), 343–353. https://doi.org/10.2151/jmsj1965.74.3_343

Garcia-Benadi, A., Bech, J., Gonzalez, S., Udina, M., Codina, B., & Georgis, J.-F. (2020). Precipitation type classification of micro rain radar data using an improved Doppler spectral processing methodology. *Remote Sensing*, *12*(24), 4113. https://doi.org/10.3390/rs12244113

Gatlin, P. N., Petersen, W. A., Knupp, K. R., & Carey, L. D. (2018). Observed response of the raindrop size distribution to changes in the melting layer. *Atmosphere*, *9*(8), 319. https://doi.org/10.3390/atmos9080319

Gelaro, R., McCarty, W., Suárez, M. J., Todling, R., Molod, A., Takacs, L., et al. (2017). The modern-era retrospective analysis for research and applications, version 2 (MERRA-2). *Journal of Climate*, *30*(14), 5419–5454. https://doi.org/10.1175/jcli-d-16-0758.1

Giangrande, S. E., Krause, J. M., & Ryzhkov, A. V. (2008). Automatic designation of the melting layer with a polarimetric prototype of the WSR-88D radar. *Journal of Applied Meteorology and Climatology*, *47*(5), 1354–1364. https://doi.org/10.1175/2007jamc1634.1

Gorodetskaya, I. V., Tsukernik, M., Claes, K., Ralph, M. F., Neff, W. D., & Van Lipzig, N. P. (2014). The role of atmospheric rivers in anomalous snow accumulation in east Antarctica. *Geophysical Research Letters*, *41*(17), 6199–6206. https://doi.org/10.1002/2014gl060881

Harpold, A. A., Kaplan, M. L., Klos, P. Z., Link, T., McNamara, J. P., Rajagopal, S., et al. (2017). Rain or snow: Hydrologic processes, observations, prediction, and research needs. *Hydrology and Earth System Sciences*, *21*(1), 1–22. https://doi.org/10.5194/hess-21-1-2017

Haynes, J. M., L'Ecuyer, T. S., Stephens, G. L., Miller, S. D., Mitrescu, C., Wood, N. B., & Tanelli, S. (2009). Rainfall retrieval over the ocean with spaceborne W-band radar. *Journal of Geophysical Research*, *114*(D8), D00A22. https://doi.org/10.1029/2008jd009973

Helmus, J. J., & Collis, S. M. (2016). The python arm radar toolkit (Py-ART), a library for working with weather radar data in the python programming language. *Journal of Open Research Software*, *4*(1), 25. https://doi.org/10.5334/jors.119

Henn, B., Weihs, R., Martin, A. C., Ralph, F. M., & Osborne, T. (2020). Skill of rain–snow level forecasts for landfalling atmospheric rivers: A multimodel assessment using California's network of vertically profiling radars. *Journal of Hydrometeorology*, *21*(4), 751–771. https://doi.org/10.1175/jhm-d-18-0212.1

Hersbach, H., Bell, B., Berrisford, P., Hirahara, S., Horányi, A., Muñoz-Sabater, J., et al. (2020). The ERA5 global reanalysis. *Quarterly Journal of the Royal Meteorological Society*, *146*(730), 1999–2049. https://doi.org/10.1002/qj.3803

Heymsfield, A. J., Bansemer, A., Theis, A., & Schmitt, C. (2021). Survival of snow in the melting layer: Relative humidity influence. *Journal of the Atmospheric Sciences*, *78*(6), 1823–1845. https://doi.org/10.1175/jas-d-20-0353.1

Hirose, M., Shige, S., Kubota, T., Furuzawa, F. A., Minda, H., & Masunaga, H. (2021). Refinement of surface precipitation estimates for the dual-frequency precipitation radar on the GPM core observatory using near-nadir measurements. *Journal of the Meteorological Society of Japan. Series II*, *99*(5), 1231–1252. https://doi.org/10.2151/jmsj.2021-060

Hou, A. Y., Kakar, R. K., Neeck, S., Azarbarzin, A. A., Kummerow, C. D., Kojima, M., et al. (2014). The global precipitation measurement mission. *Bulletin of the American Meteorological Society*, *95*(5), 701–722. https://doi.org/10.1175/bams-d-13-00164.1

Illingworth, A. J., Barker, H., Beljaars, A., Ceccaldi, M., Chepfer, H., Clerbaux, N., et al. (2015). The Earthcare satellite: The next step forward in global measurements of clouds, aerosols, precipitation, and radiation. *Bulletin of the American Meteorological Society*, *96*(8), 1311–1332. https://doi.org/10.1175/bams-d-12-00227.1

Jennings, K. S., Winchell, T. S., Livneh, B., & Molotch, N. P. (2018). Spatial variation of the rain–snow temperature threshold across the northern hemisphere. *Nature Communications*, *9*(1), 1–9. https://doi.org/10.1038/s41467-018-03629-7

Klugmann, D., Heinsohn, K., & Kirtzel, H.-J. (1996). A low cost 24 GHZ FMCW Doppler radar rain profiler. *Contributions to Atmospheric Physics/Beitraege zur Physik der Atmosphaere*, *61*(9), 247–253.

Kneifel, S., Maahn, M., Peters, G., & Simmer, C. (2011). Observation of snowfall with a low-power FM-CW k-band radar (micro rain radar). *Meteorology and Atmospheric Physics*, *113*(1), 75–87. https://doi.org/10.1007/s00703-011-0142-z

Knowles, N., Dettinger, M. D., & Cayan, D. R. (2006). Trends in snowfall versus rainfall in the Western United States. *Journal of Climate*, *19*(18), 4545–4559. https://doi.org/10.1175/jcli3850.1

Kulie, M. S., Pettersen, C., Merrelli, A. J., Wagner, T. J., Wood, N. B., Dutter, M., et al. (2021). Snowfall in the northern great lakes: Lessons learned from a multisensor observatory. *Bulletin of the American Meteorological Society*, *102*(7), E1317–E1339. https://doi.org/10.1175/bams-d-19-0128.1

Lamb, D., & Verlinde, J. (2011). Cold clouds. In *Physics and chemistry of clouds* (pp. 457–479). Cambridge University Press. https://doi.org/10.1017/CBO9780511976377.013

Le, M., Chandrasekar, V., & Biswas, S. (2016). Evaluation and validation of GPM dual-frequency classification module after launch. *Journal of Atmospheric and Oceanic Technology*, *33*(12), 2699–2716. https://doi.org/10.1175/jtech-d-15-0253.1

Lebsock, M. D., L'Ecuyer, T. S., Wood, N. B., Haynes, J. M., & Smalley, M. A. (2020). Status of the cloudsat mission. In *Satellite precipitation measurement* (pp. 25–43). Springer.

Lee, J.-E., Jung, S.-H., & Kwon, S. (2020). Characteristics of the bright band based on quasi-vertical profiles of polarimetric observations from an S-band weather radar network. *Remote Sensing*, *12*(24), 4061. https://doi.org/10.3390/rs12244061

Licznar, P., & Krajewski, W. F. (2016). Precipitation type specific radar reflectivity-rain rate relationships for Warsaw, Poland. *Acta Geophysica*, *64*(5), 1840–1857. https://doi.org/10.1515/acgeo-2016-0071

Lin, D., Pickering, B., & Neely, R. R. (2020). Relating the radar bright band and its strength to surface rainfall rate using an automated approach. *Journal of Hydrometeorology*, *21*(2), 335–353. https://doi.org/10.1175/jhm-d-19-0085.1

List, R., & Gillespie, J. (1976). Evolution of raindrop spectra with collision-induced breakup. *Journal of the Atmospheric Sciences*, *33*(10), 2007–2013. https://doi.org/10.1175/1520-0469(1976)033<2007:eorswc>2.0.co;2

Liu, G. (2008). Deriving snow cloud characteristics from cloudsat observations. *Journal of Geophysical Research*, *113*(D8), D00A09. https://doi.org/10.1029/2007jd009766

Lundquist, J. D., Neiman, P. J., Martner, B., White, A. B., Gottas, D. J., & Ralph, F. M. (2008). Rain versus snow in the Sierra Nevada, California: Comparing Doppler profiling radar and surface observations of melting level. *Journal of Hydrometeorology*, *9*(2), 194–211. https://doi.org/10.1175/2007jhm853.1

Maahn, M., Burgard, C., Crewell, S., Gorodetskaya, I. V., Kneifel, S., Lhermitte, S., et al. (2014). How does the spaceborne radar blind zone affect derived surface snowfall statistics in polar regions? *Journal of Geophysical Research: Atmospheres*, *119*(24), 13–604. https://doi.org/10.1002/2014jd022079

Maahn, M., & Kollias, P. (2012). Improved micro rain radar snow measurements using Doppler spectra post-processing. *Atmospheric Measurement Techniques*, *5*(11), 2661–2673. https://doi.org/10.5194/amt-5-2661-2012

Martner, B. E., Yuter, S. E., White, A. B., Matrosov, S. Y., Kingsmill, D. E., & Ralph, F. M. (2008). Raindrop size distributions and rain characteristics in California coastal rainfall for periods with and without a radar bright band. *Journal of Hydrometeorology*, *9*(3), 408–425. https://doi.org/10.1175/2007jhm924.1

Mateling, M. E., Pettersen, C., Kulie, M. S., Mattingly, K. S., Henderson, S. A., & L'Ecuyer, T. S. (2021). The influence of atmospheric rivers on cold-season precipitation in the upper great lakes region. *Journal of Geophysical Research: Atmospheres*, *126*(13), e2021JD034754. https://doi.org/10.1029/2021jd034754

Matrosov, S. Y. (2010). Cloudsat studies of stratiform precipitation systems observed in the vicinity of the southern great plains atmospheric radiation measurement site. *Journal of Applied Meteorology and Climatology*, *49*(8), 1756–1765. https://doi.org/10.1175/2010jamc2444.1

Matrosov, S. Y., Cifelli, R., White, A., & Coleman, T. (2017). Snow-level estimates using operational polarimetric weather radar measurements. *Journal of Hydrometeorology*, *18*(4), 1009–1019. https://doi.org/10.1175/jhm-d-16-0238.1

Matsuo, T., & Sasyo, Y. (1981). Melting of snowflakes below freezing level in the atmosphere. *Journal of the Meteorological Society of Japan. Series II*, *59*(1), 10–25. https://doi.org/10.2151/jmsj1965.59.1_10

McIlhattan, E. A., Pettersen, C., Wood, N. B., & L'Ecuyer, T. S. (2020). Satellite observations of snowfall regimes over the Greenland Ice Sheet. *The Cryosphere*, *14*(12), 4379–4404. https://doi.org/10.5194/tc-14-4379-2020

Meneghini, R., Iguchi, T., Seto, S., Yoshida, N., Awaka, J., & Kubota, T. (2021). GPM/Dpr level 2 algorithm theoretical basis document (atbd).

Newman, A. J., Kucera, P. A., & Bliven, L. F. (2009). Presenting the snowflake video imager (SVI). *Journal of Atmospheric and Oceanic Technology*, *26*(2), 167–179. https://doi.org/10.1175/2008jtecha1148.1

Norin, L., Devasthale, A., L'Ecuyer, T., Wood, N., & Smalley, M. (2015). Intercomparison of snowfall estimates derived from the cloudsat cloud profiling radar and the ground-based weather radar network over Sweden. *Atmospheric Measurement Techniques*, *8*(12), 5009–5021. https://doi.org/10.5194/amt-8-5009-2015

Norin, L., Devasthale, A., & L'Ecuyer, T. S. (2017). The sensitivity of snowfall to weather states over Sweden. *Atmospheric Measurement Techniques*, *10*(9), 3249–3263. https://doi.org/10.5194/amt-10-3249-2017

NWS. (2015). *Ncrfc zr display (Vol. date of access = Dec 2021)*. NOAA's National Weather Service. Retrieved from https://www.weather.gov/ncrfc/LMI_WOF_ZRDisplay

Pejcic, V., Saavedra Garfias, P., Mühlbauer, K., Trömel, S., & Simmer, C. (2020). Comparison between precipitation estimates of ground-based weather radar composites and GPM'S DPR rainfall product over Germany.

Perry, L. B., Seimon, A., Andrade-Flores, M. F., Endries, J. L., Yuter, S. E., Velarde, F., et al. (2017). Characteristics of precipitating storms in glacierized tropical andean cordilleras of Peru and Bolivia. *Annals of the Association of American Geographers*, *107*(2), 309–322. https://doi.org/10.1080/24694452.2016.1260439

Peters, G., Fischer, B., & Andersson, T. (2002). Rain observations with a vertically looking micro rain radar (MRR). *Boreal Environment Research*, *7*(4), 353–362.

Pettersen, C., Bliven, L. F., Kulie, M. S., Wood, N. B., Shates, J. A., Anderson, J., et al. (2021). The precipitation imaging package: Phase partitioning capabilities. *Remote Sensing*, *13*(11), 2183. https://doi.org/10.3390/rs13112183

Pettersen, C., Bliven, L. F., von Lerber, A., Wood, N. B., Kulie, M. S., Mateling, M. E., et al. (2020). The precipitation imaging package: Assessment of microphysical and bulk characteristics of snow. *Atmosphere*, *11*(8), 785. https://doi.org/10.3390/atmos11080785

Pettersen, C., Kulie, M. S., Bliven, L. F., Merrelli, A. J., Petersen, W. A., Wagner, T. J., et al. (2020). A composite analysis of snowfall modes from four winter seasons in Marquette, Michigan. *Journal of Applied Meteorology and Climatology*, *59*(1), 103–124. https://doi.org/10.1175/jamc-d-19-0099.1

Petty, G. W. (2008). *A first course in atmospheric thermodynamics*. Sundog Publishing.

Pfaff, T., Engelbrecht, A., & Seidel, J. (2014). Detection of the bright band with a vertically pointing k-bandradar.

Prein, A. F., & Heymsfield, A. J. (2020). Increased melting level height impacts surface precipitation phase and intensity. *Nature Climate Change*, *10*(8), 771–776. https://doi.org/10.1038/s41558-020-0825-x

Ryzhkov, A. V., & Zrnic, D. S. (2019). *Radar polarimetry for weather observations* (Vol. 486). Springer.

Sankaré, H., & Thériault, J. M. (2016). On the relationship between the snowflake type aloft and the surface precipitation types at temperatures near 0° c. *Atmospheric Research*, *180*, 287–296. https://doi.org/10.1016/j.atmosres.2016.06.003

Schauwecker, S., Rohrer, M., Huggel, C., Endries, J., Montoya, N., Neukom, R., et al. (2017). The freezing level in the tropical andes, Peru: An indicator for present and future glacier extents. *Journal of Geophysical Research: Atmospheres*, *122*(10), 5172–5189. https://doi.org/10.1002/2016jd025943

Schirle, C. E., Cooper, S. J., Wolff, M. A., Pettersen, C., Wood, N. B., L'Ecuyer, T. S., et al. (2019). Estimation of snowfall properties at a mountainous site in Norway using combined radar and in situ microphysical observations. *Journal of Applied Meteorology and Climatology*, *58*(6), 1337–1352. https://doi.org/10.1175/jamc-d-18-0281.1

Screen, J. A., & Simmonds, I. (2012). Declining summer snowfall in the arctic: Causes, impacts and feedbacks. *Climate Dynamics*, *38*(11), 2243–2256. https://doi.org/10.1007/s00382-011-1105-2

Serio, M. A., Carollo, F. G., & Ferro, V. (2019). Raindrop size distribution and terminal velocity for rainfall erosivity studies. A review. *Journal of Hydrology*, *576*, 210–228. https://doi.org/10.1016/j.jhydrol.2019.06.040

Shates, J. A., Pettersen, C., L'Ecuyer, T., & Kulie, M. (2022). *Ground-based remote sensing observations at Marquette*. Zenodo. https://doi.org/10.5281/zenodo.7325232

Shates, J. A., Pettersen, C., L'Ecuyer, T. S., Cooper, S. J., Kulie, M. S., & Wood, N. B. (2021). High-latitude precipitation: Snowfall regimes at two distinct sites in scandinavia. *Journal of Applied Meteorology and Climatology*, *60*(8), 1127–1148. https://doi.org/10.1175/jamc-d-20-0248.1

Sims, E. M., & Liu, G. (2015). A parameterization of the probability of snow–rain transition. *Journal of Hydrometeorology*, *16*(4), 1466–1477. https://doi.org/10.1175/jhm-d-14-0211.1

Skofronick-Jackson, G., Hudak, D., Petersen, W., Nesbitt, S. W., Chandrasekar, V., Durden, S., et al. (2015). Global precipitation measurement cold season precipitation experiment (GCPEx): For measurement's sake, let it snow. *Bulletin of the American Meteorological Society*, *96*(10), 1719–1741. https://doi.org/10.1175/bams-d-13-00262.1

Skofronick-Jackson, G., Kulie, M., Milani, L., Munchak, S. J., Wood, N. B., & Levizzani, V. (2019). Satellite estimation of falling snow: A global precipitation measurement (GPM) core observatory perspective. *Journal of Applied Meteorology and Climatology*, *58*(7), 1429–1448. https://doi.org/10.1175/jamc-d-18-0124.1

Skofronick-Jackson, G., Petersen, W. A., Berg, W., Kidd, C., Stocker, E. F., Kirschbaum, D. B., et al. (2017). The global precipitation measurement (GPM) mission for science and society. *Bulletin of the American Meteorological Society*, *98*(8), 1679–1695. https://doi.org/10.1175/bams-d-15-00306.1

Slinskey, E. A., Loikith, P. C., Waliser, D. E., Guan, B., & Martin, A. (2020). A climatology of atmospheric rivers and associated precipitation for the seven us national climate assessment regions. *Journal of Hydrometeorology*, *21*(11), 2439–2456. https://doi.org/10.1175/jhm-d-20-0039.1

Steiner, M., Smith, J. A., & Uijlenhoet, R. (2004). A microphysical interpretation of radar reflectivity–rain rate relationships. *Journal of the Atmospheric Sciences*, *61*(10), 1114–1131. https://doi.org/10.1175/1520-0469(2004)061<1114:amiorr>2.0.co;2

Stephens, G. L., Vane, D. G., Tanelli, S., Im, E., Durden, S., Rokey, M., et al. (2008). Cloudsat mission: Performance and early science after the first year of operation. *Journal of Geophysical Research*, *113*(D8), D00A18. https://doi.org/10.1029/2008jd009982

Stewart, R. E., Thériault, J. M., & Henson, W. (2015). On the characteristics of and processes producing winter precipitation types near 0°C. *Bulletin of the American Meteorological Society*, *96*(4), 623–639. https://doi.org/10.1175/bams-d-14-00032.1

Tamang, S. K., Ebtehaj, A. M., Prein, A. F., & Heymsfield, A. J. (2020). Linking global changes of snowfall and wet-bulb temperature. *Journal of Climate*, *33*(1), 39–59. https://doi.org/10.1175/jcli-d-19-0254.1

Tobin, D. M., Kumjian, M. R., & Black, A. W. (2021). Effects of precipitation type on crash relative risk estimates in Kansas. *Accident Analysis and Prevention*, *151*, 105946. https://doi.org/10.1016/j.aap.2020.105946

Uplinger, W. (1981). A new formula for raindrop terminal velocity. In *Conference on radar meteorology* (20 th, pp. 389–391).

Valdivia, J. M., Gatlin, P. N., Kumar, S., Scipión, D., Silva, Y., & Petersen, W. A. (2022). The gpm-dpr blind zone effect on satellite-based radar estimation of precipitation over the Andes from a ground-based ka-band profiler perspective. *Journal of Applied Meteorology and Climatology*, *61*(4), 441–456. https://doi.org/10.1175/jamc-d-20-0211.1

von Lerber, A., Moisseev, D., Leinonen, J., Koistinen, J., & Hallikainen, M. T. (2014). Modeling radar attenuation by a low melting layer with optimized model parameters at C-band. *IEEE Transactions on Geoscience and Remote Sensing*, *53*(2), 724–737. https://doi.org/10.1109/tgrs.2014.2327148

Wang, P., & Pruppacher, H. (1977). Acceleration to terminal velocity of cloud and raindrops. *Journal of Applied Meteorology*, *16*(3), 275–280. https://doi.org/10.1175/1520-0450(1977)016<0275:attvoc>2.0.co;2

Watters, D., Battaglia, A., Mroz, K., & Tridon, F. (2018). Validation of the GPM version-5 surface rainfall products over Great Britain and Ireland. *Journal of Hydrometeorology*, *19*(10), 1617–1636. https://doi.org/10.1175/jhm-d-18-0051.1

White, A. B., Gottas, D. J., Strem, E. T., Ralph, F. M., & Neiman, P. J. (2002). An automated brightband height detection algorithm for use with Doppler radar spectral moments. *Journal of Atmospheric and Oceanic Technology*, *19*(5), 687–697. https://doi.org/10.1175/1520-0426(2002)019<0687:aabhda>2.0.co;2

Williams, C. R., Ecklund, W. L., & Gage, K. S. (1995). Classification of precipitating clouds in the tropics using 915-mhz wind profilers. *Journal of Atmospheric and Oceanic Technology*, *12*(5), 996–1012. https://doi.org/10.1175/1520-0426(1995)012<0996:copcit>2.0.co;2

You, Y., Peters-Lidard, C., Ringerud, S., & Haynes, J. M. (2021). Evaluation of rainfall-snowfall separation performance in remote sensing datasets. *Geophysical Research Letters*, *48*(21), e2021GL094180. https://doi.org/10.1029/2021gl094180

Yuter, S. E., Kingsmill, D. E., Nance, L. B., & Löffler-Mang, M. (2006). Observations of precipitation size and fall speed characteristics within coexisting rain and wet snow. *Journal of Applied Meteorology and Climatology*, *45*(10), 1450–1464. https://doi.org/10.1175/jam2406.1